Comparison of finite difference and boundary integral solutions to three-dimensional spontaneous rupture

Steven M. Day and Luis A. Dalguer
Department of Geological Sciences, San Diego State University, San Diego, California, USA

Nadia Lapusta
Division of Engineering and Applied Science and Division of Geological and Planetary Sciences, California Institute of Technology, Pasadena, California, USA

Yi Liu
Division of Engineering and Applied Science, California Institute of Technology, Pasadena, California, USA

Received 2 May 2005; revised 5 October 2005; accepted 12 October 2005; published 23 December 2005.

[1] The spontaneously propagating shear crack on a frictional interface has proven to be a useful idealization of a natural earthquake. The corresponding boundary value problems are nonlinear and usually require computationally intensive numerical methods for their solution. Assessing the convergence and accuracy of the numerical methods is challenging, as we lack appropriate analytical solutions for comparison. As a complement to other methods of assessment, we compare solutions obtained by two independent numerical methods, a finite difference method and a boundary integral (BI) method. The finite difference implementation, called DFM, uses a traction-at-split-node formulation of the fault discontinuity. The BI implementation employs spectral representation of the stress transfer functional. The three-dimensional (3-D) test problem involves spontaneous rupture spreading on a planar interface governed by linear slip-weakening friction that essentially defines a cohesive law. To get a priori understanding of the spatial resolution that would be required in this and similar problems, we review and combine some simple estimates of the cohesive zone sizes which correspond quite well to the sizes observed in simulations. We have assessed agreement between the methods in terms of the RMS differences in rupture time, final slip, and peak slip rate and related these to median and minimum measures of the cohesive zone resolution observed in the numerical solutions. The BI and DFM methods give virtually indistinguishable solutions to the 3-D spontaneous rupture test problem when their grid spacing Δx is small enough so that the solutions adequately resolve the cohesive zone, with at least three points for BI and at least five node points for DFM. Furthermore, grid-dependent differences in the results, for each of the two methods taken separately, decay as a power law in Δx, with the same convergence rate for each method, the calculations apparently converging to a common, grid interval invariant solution. This result provides strong evidence for the accuracy of both methods. In addition, the specific solution presented here, by virtue of being demonstrably grid-independent and consistent between two very different numerical methods, may prove useful for testing new numerical methods for spontaneous rupture problems.

Citation: Day, S. M., L. A. Dalguer, N. Lapusta, and Y. Liu (2005), Comparison of finite difference and boundary integral solutions to three-dimensional spontaneous rupture, *J. Geophys. Res.*, *110*, B12307, doi:10.1029/2005JB003813.

1. Introduction

[2] The shear crack, propagating spontaneously under the influence of assumed initial stresses, and sliding under a specified friction law, is a useful, if highly simplified, model of a natural earthquake. Even when the rupture is idealized as a discontinuity surface embedded in an otherwise linearly elastic continuum, the spontaneous rupture problem is highly nonlinear. The nonlinearity is attributable to the fact that rupture evolution and arrest are determined as part of the problem solution, not specified a priori. That is, the problem is a mixed boundary value problem in which the respective (time-dependent) domains of the kinematic and dynamic boundary conditions have to be determined as part of the problem solution itself. There are no analytical

0148-0227/05/2005JB003813$09.00

solutions to problems of this class, and we must rely heavily upon numerical solutions for insight into the behavior of this model of the earthquake process.

[3] The challenge of validating numerical methods for the solution of spontaneous rupture problems, in the absence of analytical solutions for reference, was discussed by *Day and Ely* [2002]. As they point out, the achievement of nearly identical numerical results using progressively finer discretization of the domain, while important, may not be sufficient to prove accuracy in this class of problems. Day and Ely took an experimental approach to validation, using scale model earthquake experiments of *Brune and Anooshehpoor* [1998] to test the finite difference method of *Day* [1982b]. Day and Ely's numerical simulations of those experiments incorporated the geometry and experimentally measured bulk and surface properties of the sliding blocks and then reproduced the timing, shape and duration of acceleration pulses recorded adjacent to the experimental fault surface. While the comparison provided indirect evidence about the accuracy of the numerical procedure, it could not measure the accuracy of the numerical method separately from adjustments to constitutive parameters and other modeling considerations.

[4] In this paper, we offer another approach to assessing the accuracy of numerical solutions. We compare 3-D solutions obtained by two independent numerical methods, a finite difference method and a boundary integral (BI) method. In the absence of a strict mathematical proof that either method converges to an exact solution for spontaneous rupture problems, this comparison provides validation for both numerical approaches, because these numerical methods have a high degree of independence. The BI method might, in fact, be appropriately called a semianalytical method, because it discretizes only the fault surface points; the reaction of the continuum to slip at those points is represented exactly, through a closed form Green's function. In contrast, the finite difference method uses a volume discretization to approximate the differential equations of motion throughout the 3-D problem domain. *Bizzarri et al.* [2001] made similar comparisons of finite difference and BI solutions to 2-D rupture problems. The semianalytical character of the BI method restricts its applicability to problems in which the fault surface is embedded in a uniform infinite space, but renders it highly efficient and accurate for solving such geometrically limited problems and hence suitable for confirming the accuracy of the finite difference method. The finite difference method, while much more flexible than the BI method, is susceptible to numerical limitations such as numerical dispersion that do not beset the latter.

2. Theoretical Formulation

[5] We treat the problem of an isotropic, linearly elastic infinite space containing a surface Σ across which the displacement vector may have a discontinuity. The linearized equations of motion for the space are

$$\boldsymbol{\sigma} = \rho\left(\alpha^2 - 2\beta^2\right)(\nabla \cdot \mathbf{u})\mathbf{I} + \rho\beta^2(\nabla\mathbf{u} + \mathbf{u}\nabla) \tag{1a}$$

$$\ddot{\mathbf{u}} = \rho^{-1}\nabla \cdot \sigma, \tag{1b}$$

in which $\boldsymbol{\sigma}$ is the stress tensor, $\mathbf{u}$ is the displacement vector, α and β are the P and S wave speeds, respectively, ρ is density, and $\mathbf{I}$ is the identity tensor.

[6] The surface Σ has a (continuous) unit normal vector $\hat{\mathbf{n}}$. A discontinuity in the displacement vector is permitted across the interface Σ. On Σ we define limiting values of the displacement vector, $\mathbf{u}^+$ and $\mathbf{u}^-$, by

$$\mathbf{u}^{\pm}(\mathbf{x}, t) = \lim_{\varepsilon \to 0} \mathbf{u}(\mathbf{x} \pm \varepsilon\hat{\mathbf{n}}(\mathbf{x}), t) \tag{2}$$

(in this linearized theory, we can neglect the time dependence of $\hat{\mathbf{n}}$). We denote the discontinuity of the vector of tangential displacement (i.e., the "slip") by $\mathbf{s} \equiv (\mathbf{I} - \hat{\mathbf{n}}\hat{\mathbf{n}}) \cdot (\mathbf{u}^+ - \mathbf{u}^-)$, its time derivative (the "slip rate") by $\dot{\mathbf{s}}$, and their magnitudes by s and $\dot{s}$, respectively. The traction vector $\boldsymbol{\sigma} \cdot \hat{\mathbf{n}}$ is continuous across Σ. The shear traction vector $\boldsymbol{\tau}$ is given by $(\mathbf{I} - \hat{\mathbf{n}}\hat{\mathbf{n}}) \cdot \boldsymbol{\sigma} \cdot \hat{\mathbf{n}}$, and its magnitude τ is bounded above by a nonnegative frictional strength τ_c.

[7] We formulate the jump conditions at the interface as

$$\tau_c - \tau \geq 0 \tag{3}$$

$$\tau_c\dot{\mathbf{s}} - \boldsymbol{\tau}\dot{s} = 0. \tag{4}$$

Equation (3) stipulates that the shear traction be bounded by the (current value of) frictional strength, and equation (4) stipulates that any nonzero velocity discontinuity be opposed by an antiparallel traction (i.e., the negative side exerts traction $-\boldsymbol{\tau}$ on the positive side) with magnitude equal to the frictional strength τ_c. However, note that (4) has been written in a form such that it remains valid when $\dot{s}$ is zero. In fact, when equality does not pertain in (3), (4) can be satisfied only with $\dot{s}$ equal to zero.

[8] The frictional strength evolves according to some constitutive functional which may in principle depend upon the history of the velocity discontinuity, and any number of other mechanical or thermal quantities, but is here simplified to the well-known slip-weakening form, introduced by *Ida* [1972] and *Palmer and Rice* [1973] by analogy to cohesive zone models of tensile fracture. In that form, τ_c is the product of compressive normal stress $-\sigma_n$ (as $\sigma_n \equiv \hat{\mathbf{n}} \cdot \boldsymbol{\sigma} \cdot \hat{\mathbf{n}}$ is positive in tension) and a coefficient of friction $\mu_f(\ell)$ that depends on the slip path length ℓ given by $\int_0^t \dot{s}(t')\, dt'$,

$$\tau_c = -\sigma_n\mu_f(\ell). \tag{5}$$

We use the linear slip-weakening form in which μ_f is given by

$$\mu_f(\ell) = \begin{cases} \mu_s - (\mu_s - \mu_d)\ell/d_0 & \ell < d_0 \\ \mu_d & \ell \geq d_0, \end{cases} \tag{6}$$

where μ_s and μ_d are coefficients of static and dynamic friction, respectively, and d_0 is the critical slip-weakening distance [e.g., *Ida*, 1972; *Andrews*, 1976; *Day*, 1982b, *Madariaga et al.*, 1998, *Dalguer et al.*, 2001]. In the event that the normal stress and frictional parameters are constant over the entire fault, as will be the case in the test problem considered here, this idealized model results in constant

fracture energy Γ with $\Gamma = |\sigma_n|(\mu_s - \mu_d)d_0/2$. This simple model provides an adequate basis for testing the numerical methods, though it may have significant shortcomings as a model for earthquakes, in which interface frictional properties may be better represented by more complicated relationships that account for rate and state effects [e.g., *Dieterich*, 1979; *Ruina*, 1983] and thermal phenomena such as flash heating and pore pressure evolution [e.g., *Lachenbruch*, 1980; *Mase and Smith*, 1985, 1987; *Rice*, 1999]. Moreover, the energy dissipation may not be confined mostly to the fracture surface, but rather distributed in a damage zone of finite thickness around the surface [e.g., *Andrews*, 1976, 2005; *Dalguer et al.*, 2003a, 2003b].

[9] Jump conditions (3)–(4), combined with the friction law (5)–(6) and appropriate initial stress conditions on Σ, provide a model of fault behavior which is complete in the sense that no memory variables have to be specified to explicitly track the state of rupture at each point. That is, these conditions alone can model initial rupture (when the initial transition from inequality to equality occurs in (3)), arrest of sliding (when (3) undergoes a transition from equality back to inequality), and reactivation of slip (if condition 3 switches back again from inequality to equality).

[10] In the test problems considered here, the problem symmetries preclude the normal stress on the fault from fluctuating from its initial value during the rupture process. Thus tensile motion (interface separation) does not occur. For the sake of completeness, however, we also describe an extension of the set of jump conditions appropriate to the more general problem in which normal stress fluctuations are present. In that case, the interface may undergo separation over portions of the contact surface Σ if there is a transient reduction of the compressive normal stress to zero [*Day*, 1991]. We denote the normal component of the displacement discontinuity on Σ by U_n, with jump conditions

$$\sigma_n \leq 0, \tag{7}$$

$$U_n \geq 0, \tag{8}$$

$$\sigma_n U_n = 0, \tag{9}$$

corresponding to nontensile normal stress, no interpenetration, and loss of contact only if accompanied by zero normal stress, respectively. Again, these jump conditions are adequate to cover multiple episodes of tensile rupture and crack closure, without need for any memory variables to track the state of rupture. (To model a nonzero tensile limit $\sigma_{\max} > 0$, σ_n is just replaced by $\sigma_n - \sigma_{\max}$ in conditions (7) and (9).)

3. Finite Difference Method

[11] Several different finite difference methods have been used to solve the spontaneous rupture problem [e.g., *Andrews*, 1976; *Miyatake*, 1980; *Day*, 1982b; *Madariaga et al.*, 1998]. These have been limited for the most part to faults consisting of planar segments, although a few recent solutions are for nonplanar faults [e.g., *Cruz-Atienza and Virieux*, 2004; *Kase and Day*, 2004; *Zhang et al.*, 2004]. An important factor influencing the accuracy of these methods is the technique used to represent the displacement discontinuity and traction at the fault plane [*Andrews*, 1999; *Dalguer and Day*, 2004]. Here we use the finite difference method of *Day* [1982b], which incorporates what *Andrews* [1999] has called the traction-at-split-node (TSN) method to treat the displacement discontinuity. It has recently been recoded for modern high-performance multiprocessor clusters, using message passing (MPI) to implement concurrency [*Ely*, 2001]. This version of the code is called dynamic fault model (DFM), and here we will use that abbreviation to refer to our implementation of the TSN finite difference method. The same method was used in the experimental tests of *Day and Ely* [2002].

[12] The DFM method approximates the displacement field on a Cartesian, tensor product mesh; i.e., the (rectangular) unit cell indexed j, k, l has dimensions Δx_j, Δy_k, Δz_l, where the Δx_j, etc, can be assigned arbitrarily. The problem domain is thus a rectangular prism with six boundary surfaces. On each boundary surface, either fixed or free conditions may be separately specified for each component of motion. The method solves rupture problems for infinite (or semi-infinite) domains by placing the appropriate mesh boundaries sufficiently remote from the rupture surface that they produce no reflections within some space-time subdomain of interest. The material properties of the volume are isotropic, but may be heterogeneous. Each subvolume may be elastic, Kelvin-Voigt viscoelastic (used principally as a regularization device to selectively damp high-frequency components), or elastoplastic.

[13] The spatial difference operators were constructed by specializing trilinear elastic finite elements to the Cartesian mesh, approximating integrals by one-point quadrature, and diagonalizing the mass matrix (see Appendix A). The method approximates temporal derivatives by explicit, central differencing in time. On a uniform mesh, the method is second-order accurate in space and time. In that case, the differencing scheme that results from this procedure is equivalent (away from the fault surface) to the second-order partly staggered grid method, which has been reviewed by *Moczo et al.* [2006] [see also *Abramowitz and Stegun*, 1964, p. 884, formula 25.3.22].

[14] The numerical representation of the jump conditions (3) and (4) used in *Day*'s [1982b] split node treatment has been described piecemeal in other publications [*Day*, 1977; *Archuleta and Day*, 1980] and was reviewed more systematically by *Andrews* [1999]. For completeness, and to provide a unified exposition of the shear and tensile faulting cases, we describe the method in detail here.

[15] Split nodes define the faults, on which all three components of displacement (and velocity) may have discontinuities. Any number of faults is permitted, but each must coincide with a coordinate plane (the faults collectively forming a single family of parallel planes). Figure 1 illustrates the basic grid geometry.

[16] As shown in Figure 1, a given fault plane node is split into plus-side and minus-side parts. The two halves of a split node interact only through a traction acting on the interface between them. To give some physical content to our description, we lump together portions of the difference equations into terms that can be interpreted as forces and

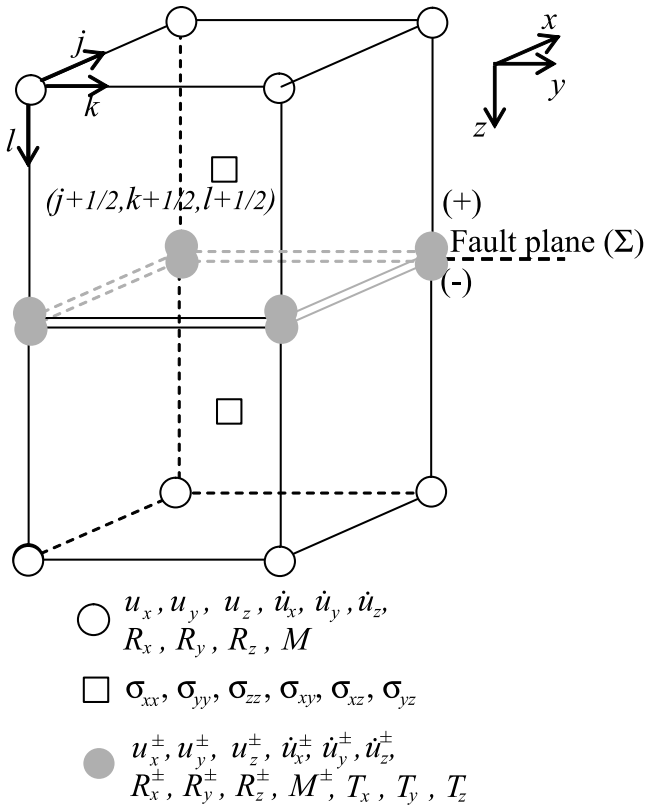

Figure 1. Split node geometry of DFM, illustrated for two cubic unit cells. Mass ($M^{\pm}$) is split, and separate elastic restoring forces ($R_\nu^{\pm}$) act on the two halves. The two halves of a split node interact only through shear and normal tractions (T_ν) at the interface.

inertias acting at the respective half nodes. The plus-side and minus-side nodes then have respective masses M^+ and M^- (as defined in Appendix A), and experience respective elastic restoring forces, R^+ and R^- (see Appendix A). The forces represent the stress divergence terms in the equations of motion but are partitioned into separate contributions from each side of the fault plane. At a particular time t, D'Alembert's principle leads to a force balance (including inertial forces) equation for each split node. This is approximated by central time differencing [e.g., *Wood*, 1990, p. 265] and integrated to estimate the nodal velocity and displacement components. Taking a minor liberty with notation, we use the same symbols to represent nodal displacement in the discrete equations as we used earlier to represent the displacement field in the theoretical formulation of the continuum problem, adding Greek subscripts to denote Cartesian components (x, y, or z), Roman subscripts to indicate nodal indices on the fault plane (which we take normal to the z axis), and a superscript to distinguish the two halves of the split nodes. In this notation, the velocity and displacement components at the split nodes, $\dot{u}_\nu^{\pm}$ and $u_\nu^{\pm}$, are

$$\left[\dot{u}_\nu^{\pm}(t+\Delta t/2)\right]_{jk} = \left[\dot{u}_\nu^{\pm}(t-\Delta t/2)\right]_{jk} + \Delta t\left(M_{jk}^{\pm}\right)^{-1} \cdot\left\{\left[R_\nu^{\pm}(t)\right]_{jk} \mp a_{jk}\left[T_\nu(t)\right]_{jk} \pm a_{jk}\left[T_\nu^0\right]_{jk}\right\} \quad (10)$$

$$\left[u_\nu^{\pm}(t+\Delta t)\right]_{jk} = \left[u_\nu^{\pm}(t)\right]_{jk} + \Delta t\left[\dot{u}_\nu^{\pm}(t+\Delta t/2)\right]_{jk},$$

where Δt is the time step, a_{jk} is the area of the fault surface associated with the split node jk, $[T_\nu]_{jk}$ is the fault plane traction vector at node jk, and $[T_\nu^0]_{jk}$ is the initial equilibrium value of $[T_\nu]_{jk}$.

[17] Next we define $(\tilde{T}_\nu)_{jk}$ as the fault plane nodal traction components that, when introduced into (10), would enforce continuity of tangential velocity ($\dot{u}_\nu^+ - \dot{u}_\nu^- = 0$ for ν equal to x and y) and continuity of normal displacement ($u_z^+ - u_z^- = 0$). The resulting expression (suppressing the node indices jk) is

$$\tilde{T}_\nu \equiv \frac{\Delta t^{-1}M^+M^-\left(\dot{u}_\nu^+ - \dot{u}_\nu^-\right) + M^-R_\nu^+ - M^+R_\nu^-}{a(M^+ + M^-)} + T_\nu^0, \quad \nu = x, y,$$

$$\tilde{T}_\nu \equiv \frac{\Delta t^{-1}M^+M^-\left[\left(\dot{u}_\nu^+ - \dot{u}_\nu^-\right) + \Delta t^{-1}\left(u_\nu^+ - u_\nu^-\right)\right] + M^-R_\nu^+ - M^+R_\nu^-}{a(M^+ + M^-)} + T_\nu^0, \quad \nu = z, \quad (11)$$

where the velocities are evaluated at $t - \Delta t/2$, and the nodal tractions, restoring forces and displacements at t. All quantities in (11) except Δt have an implied dependence on the node indices. All jump conditions on the fault are then satisfied if the fault plane traction T_ν of equation (10) is

$$T_\nu = \begin{cases} \tilde{T}_\nu & \nu = x, y, \ \left[\left(\tilde{T}_x\right)^2 + \left(\tilde{T}_y\right)^2\right]^{1/2} \le \tau_c, \\ \tau_c \dfrac{\tilde{T}_\nu}{\left[\left(\tilde{T}_x\right)^2 + \left(\tilde{T}_y\right)^2\right]^{1/2}} & \nu = x, y, \ \left[\left(\tilde{T}_x\right)^2 + \left(\tilde{T}_y\right)^2\right]^{1/2} > \tau_c, \\ \tilde{T}_\nu & \nu = z, \quad \tilde{T}_z \le 0, \\ 0 & \nu = z, \quad \tilde{T}_z \ge 0, \end{cases} \quad (12)$$

with all quantities in (12) evaluated at time t. By substitution of (12) into (10), it can be verified that the first two equalities of equation (12) enforce the shear jump conditions on the fault, conditions (3) and (4), in the discrete form

$$\tau_c(t) - \left[T_x^2(t) + T_y^2(t)\right]^{1/2} \ge 0, \quad (13)$$

$$\tau_c(t)\left[\dot{u}_\nu^+(t+\Delta t/2) - \dot{u}_\nu^-(t+\Delta t/2)\right] = T_\nu(t)\left\{\left[\dot{u}_x^+(t+\Delta t/2) - \dot{u}_x^-(t+\Delta t/2)\right]^2 + \left[\dot{u}_y^+(t+\Delta t/2) - \dot{u}_y^-(t+\Delta t/2)\right]^2\right\}^{1/2}, \quad \nu = x, y. \quad (14)$$

Note that the parallelism condition (14) has a $\Delta t/2$ time shift between traction and velocity. We use this form, rather than the more obvious alternative of enforcing this condition with the slip velocity averaged over times $t - \Delta t/2$ and $t + \Delta t/2$, because the latter occasionally results in spurious oscillations in rake direction near the time of rupture arrest. Likewise, the last two equalities of (12)

enforce the jump conditions for the normal components on the fault, conditions (7) to (9), in the discrete form

$$T_z(t) \le 0, \tag{15}$$

$$u_z^+(t) - u_z^-(t) \ge 0, \tag{16}$$

$$T_z(t)\left[u_z^+(t+\Delta t) - u_z^+(t+\Delta t)\right] = 0. \tag{17}$$

[18] Note that (12), combined with suitable initial conditions and the constitutive equations for τ_c, governs fault behavior (at a given point jk) at all times, including prerupture, initial rupture, arrest of sliding, and possible subsequent episodes of reactivation and arrest. With the above formulation, it is unnecessary to test for these conditions nor to construct separate fault plane equations for these different conditions.

4. Boundary Integral Method

[19] Boundary integral (BI) methods have been widely used to investigate spontaneous propagation of cracks in elastic media [e.g., *Das*, 1980; *Andrews*, 1985; *Das and Kostrov*, 1988; *Cochard and Madariaga*, 1994; *Perrin et al.*, 1995; *Geubelle and Rice*, 1995; *Ben-Zion and Rice*, 1997; *Kame and Yamashita*, 1999; *Aochi et al.*, 2000; *Lapusta et al.*, 2000; *Lapusta and Rice*, 2003]. The main idea of BI methods is to confine the numerical consideration to the crack path, by expressing the elastodynamic response of the surrounding elastic media in terms of integral relationships between displacement discontinuities and tractions along the path. These relationships involve convolutions in space and time of either displacement discontinuities and their histories or tractions and their histories. Such an approach eliminates the necessity to simulate wave propagation through elastic media, because that wave propagation is accounted for by the convolutions. The trick is then to determine the appropriate convolution kernels, which is possible to do analytically only for the simplest situations such as crack propagation in an infinite, uniform elastic solid. Mostly, crack propagation along planar interfaces has been studied. Recently, advances have been made in using BI methods to simulate crack propagation along a self-chosen path [e.g., *Kame and Yamashita*, 1999], along a network of planar paths [e.g., *Aochi et al.*, 2000], and along a planar path embedded in a half-space [e.g., *Chen and Zhang*, 2004]. More complicated problems (such as a layered elastic medium, etc.) may be possible to consider by precalculating convolution kernels numerically as briefly discussed by *Lapusta et al.* [2000], but to our knowledge this has not yet been implemented.

[20] The test problem we consider in this work involves a planar interface in an infinite uniform elastic medium. The boundary integral methods are highly efficient for such problems and show good convergence with increasing numerical resolution. Unlike for DFM, the challenge is not in simulating the wave propagation directly, but rather in computing the convolution integrals involved.

[21] We employ the spectral formulation of the boundary integral method for planar interfaces pioneered by *Perrin et al.* [1995] for two-dimensional antiplane problems and extended by *Geubelle and Rice* [1995] to three-dimensional fracture problems. The three-dimensional formulation allows for displacement discontinuities that are both normal (opening) and tangential (slip) to the crack interface. *Geubelle and Rice* [1995] applied the formulation to numerical simulations of tensile cracking. Here we adopt the formulation for the shear case, with slip only and *no opening*. Hence the displacements normal to the interface are continuous in our case.

[22] The tractions, $\tau_\nu(x, y, t) = \sigma_{z\nu}(x, y, 0, t)$, $\nu = x, y, z$ on the planar interface $z = 0$ are expressed as the sum of the "loading" tractions $\tau_\nu^0(x, y, t)$ that would act on the interface in the absence of any displacement discontinuity on that interface plus additional terms due to time-dependent relative slip (or tangential displacement discontinuities $s_\nu(x, y, t)$) on the interface, in the form

$$\tau_\nu(x,y,t) = \tau_\nu^0(x,y,t) + f_\nu(x,y,t) - \frac{\mu}{2\beta}\dot{s}_\nu(x,y,t), \quad \nu = x,y \tag{18a}$$

$$\tau_z(x,y,t) = \sigma_{zz}(x,y,0,t) = \tau_z^0(x,y,t). \tag{18b}$$

In (18a), $f_\nu(x, y, t)$ are functionals of tangential displacement discontinuities; these stress transfer functionals incorporate much of the elastodynamic response and involve convolution integrals. The last term on the right of (18a), $-(\mu/2\beta)\,\dot{s}_\nu(x, y, t)$, where μ is the shear modulus and β is the shear wave speed, is separated to reduce the singularity of the convolution integrals [*Cochard and Madariaga*, 1994]; $\dot{s}_\nu(x, y, t)$, as before, denote the time derivatives of the tangential displacement discontinuities. Equation (18b) reflects the elastodynamic fact that tangential displacement discontinuities (or slips) on a planar interface between identical elastic solids do not alter the stress normal to the interface, and hence the time dependence of normal stress in the shear case can be imposed only externally (through dynamic loading, for example). The normal stress would be altered by the displacement discontinuity normal to the interface, by nonplanarity of the sliding surface, or by sliding on a planar interface between dissimilar elastic solids. However, we do not consider any of those cases here.

[23] The loading tractions $\tau_\nu^0(x, y, t)$ are the stresses that would result along the interface due to external loading if the interface were restricted against any slip. Hence they need to be computed from the prescribed loading before the formulation (18) can be applied. In the test cases considered here, the tractions before the sliding starts are given and there is no additional loading, and hence $\tau_\nu^0(x, y, t)$ are just equal to the initial tractions prescribed. To study earthquake problems in general, one can assume some (simplified) loading scenarios, for example, one in which, $\tau_\nu^0(x, y, t)$, $\nu = x, y$, grow with time in a prescribed manner.

[24] The method is called "spectral" because it relates the functionals $f_\nu(x, y, t)$, $\nu = x, y$, to displacement discontinuities $s_\nu(x, y, t)$ in the Fourier domain. For our numerical implementation, we represent the displacement discontinu-

ities and stress transfer functionals by their truncated Fourier series. The interface is discretized into rectangular elements, with L_ν (even) being the number of elements in the ν direction, and we write

$$\begin{aligned} s_\nu(x,y,t) &= \sum_{k=-L_x/2}^{L_x/2}\sum_{m=-L_y/2}^{L_y/2} S_\nu(t;k,m)\exp\left[2\pi i\left(kx/\lambda_x + my/\lambda_y\right)\right] \\ f_\nu(x,y,t) &= \sum_{k=-L_x/2}^{L_x/2}\sum_{m=-L_y/2}^{L_y/2} F_\nu(t;k,m)\exp\left[2\pi i\left(kx/\lambda_x + my/\lambda_y\right)\right] \\ \nu &= x,y. \end{aligned} \tag{19}$$

In (19), λ_x and λ_y are the dimensions of the interface region simulated, replicated periodically. The periods λ_x and λ_y have to be chosen larger than the domain over which the rupture propagation takes place, to assure that the influence of waves arriving from the periodic replicates of the rupture process is negligible. Let us denote the wave vectors of Fourier components by $\mathbf{q} = (\hat{k}, \hat{m})$, with

$$\hat{k} = 2\pi k/\lambda_x, \quad \hat{m} = 2\pi m/\lambda_y, \quad q = \sqrt{\hat{k}^2 + \hat{m}^2}. \tag{20}$$

The Fourier coefficients $F_\nu(t; k, m)$ of the functionals and $S_\nu(t; k, m)$ of the displacement discontinuities are then related by

$$\begin{aligned} &\begin{Bmatrix} F_x(t;k,m) \\ F_y(t;k,m) \end{Bmatrix} \\ &= \frac{\mu}{2q}\begin{bmatrix} \hat{k}^2 & \hat{m}\hat{k} \\ \hat{m}\hat{k} & \hat{m}^2 \end{bmatrix}\int_0^t C_{\mathrm{II}}(q\beta t')\begin{Bmatrix} S_x(t-t';k,m) \\ S_y(t-t';k,m) \end{Bmatrix} q\beta dt' \\ &-\frac{\mu}{2q}\begin{bmatrix} \hat{m}^2 & -\hat{m}\hat{k} \\ -\hat{m}\hat{k} & \hat{k}^2 \end{bmatrix}\int_0^t C_{\mathrm{III}}(q\beta t')\begin{Bmatrix} S_x(t-t';k,m) \\ S_y(t-t';k,m) \end{Bmatrix} q\beta dt', \end{aligned} \tag{21}$$

where C_{II} and C_{III} are convolution kernels that correspond to modes II and III of the standard deformation decomposition in fracture mechanics. Equation (21) assumes that there are no displacement discontinuities before $t = 0$. The convolution kernels are

$$\begin{aligned} C_{\mathrm{II}}(T) &= J_1(T)/T + 4T\left[W\left(\frac{\alpha}{\beta}T\right) - W(T)\right] - 4\frac{\beta}{\alpha}J_o\left(\frac{\alpha}{\beta}T\right) \\ &\quad + 3J_o(T), \\ C_{\mathrm{III}}(T) &= J_1(T)/T, \quad W(T) = \int_T^\infty \frac{J_1(\xi)}{\xi}d\xi = 1 - \int_0^T \frac{J_1(\xi)}{\xi}d\xi. \end{aligned} \tag{22}$$

In equations (22), $J_0(T)$ and $J_1(T)$ denote Bessel functions.

[25] The formulation that involves expressions (21) is referred to as "displacement" formulation, because the convolutions in (21) are done on the histories of Fourier coefficients of displacement discontinuities. To separate the static (long-term) and transient dynamic responses, the integrals in (21) can be integrated by parts to obtain

$$\begin{aligned} \begin{Bmatrix} F_x(t;k,m) \\ F_y(t;k,m) \end{Bmatrix} &= -\frac{\mu}{2q}\begin{bmatrix} \hat{k}^2 & \hat{m}\hat{k} \\ \hat{m}\hat{k} & \hat{m}^2 \end{bmatrix}\left(2\left(1-\frac{\beta^2}{\alpha^2}\right)\begin{Bmatrix} S_x(t;k,m) \\ S_y(t;k,m) \end{Bmatrix}\right. \\ &\quad \left. - \int_0^t K_{\mathrm{II}}(q\beta t')\begin{Bmatrix} \dot{S}_x(t-t';k,m) \\ \dot{S}_y(t-t';k,m) \end{Bmatrix} dt'\right) \\ &\quad -\frac{\mu}{2q}\begin{bmatrix} \hat{m}^2 & -\hat{m}\hat{k} \\ -\hat{m}\hat{k} & \hat{k}^2 \end{bmatrix}\left(\begin{Bmatrix} S_x(t;k,m) \\ S_y(t;k,m) \end{Bmatrix}\right. \\ &\quad \left. - \int_0^t K_{\mathrm{III}}(q\beta t')\begin{Bmatrix} \dot{S}_x(t-t';k,m) \\ \dot{S}_y(t-t';k,m) \end{Bmatrix} dt'\right), \\ K_{\mathrm{II}}(T) &= \int_T^\infty C_{\mathrm{II}}(\xi)d\xi = 2\left(1-\frac{\beta^2}{\alpha^2}\right) - \int_0^T C_{\mathrm{II}}(\xi)d\xi, \\ K_{\mathrm{III}}(T) &= \int_T^\infty C_{\mathrm{III}}(\xi)d\xi = 1 - \int_0^T C_{\mathrm{III}}(\xi)d\xi. \end{aligned} \tag{23}$$

In this work, we use the formulation (18), (19), (22), (23), which is called the "velocity" formulation [*Perrin et al.*, 1995].

[26] The spectral BI formulation has several advantages over the purely space-time formulation. In the latter, stress transfer functionals $f_\nu(x, y, t)$ are written as integrals on both space and time, because the tractions at a particular location on the interface depend on the slip information within the relevant space-time cone determined by the speed of the propagation of elastic waves. Hence, in the discretized space-time formulation, the value of the stress transfer functional for each cell would be determined by the histories of displacement discontinuities for all relevant cells. In the spectral formulation, the Fourier coefficients of the functionals corresponding to the wave vector $\mathbf{q}$ depend only on the Fourier coefficients of the displacement discontinuity corresponding to the same vector $\mathbf{q}$, as can be seen in (21) or (23). Hence the space-related integration is eliminated at the cost of introducing Fourier transforms. However, Fourier transforms take less computational time than space integration, even when the necessity to simulate larger domains is taken into consideration, as discussed by *Lapusta et al.* [2000] for a two-dimensional case. Another advantage is having the transient elastodynamic response separated into Fourier modes. The convolution kernels in (23) are oscillating with decaying amplitude and hence at large enough times the convolutions can be truncated. In addition, the arguments of the kernels contain the magnitude of the wave vector, which is larger for higher modes. Hence the convolution for the higher modes can be truncated sooner than for the lower modes, and such mode-dependent truncation can save a lot of computational time, as discussed by *Lapusta et al.* [2000] for a 2-D case. Moreover, such mode-dependent truncation may serve as means to suppress numerical high-frequency noise, although this has not yet been studied systematically. Note that separation of the response into the static part (involving the current values of displacement discontinuities) and the dynamic part (involving convolution integrals on velocity discontinuities) as accomplished

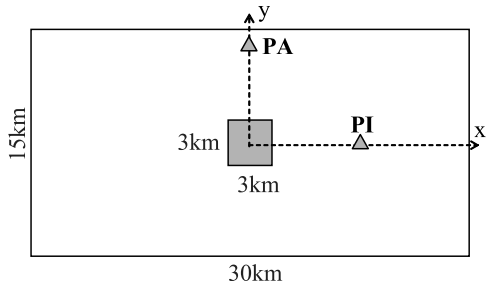

Figure 2. Fault model [from *Harris et al.*, 2004] for testing dynamic rupture simulations. The square in the center is the nucleation area. The triangles are the receivers at which we compare time histories of slip, slip rate, and shear stress. Relative to an origin at the center of the fault, the receiver PI has y coordinate 0 and x coordinate 7.5 km, and the receiver PA has x coordinate 0 and y coordinate 6.0 km. The stress parameters are specified in Table 1.

by (23) ensures that regardless of how the convolutions are truncated, the final static stress response is fully accounted for. Even though justifiable truncation produces results very close to those obtained with no truncation, we do not use truncation in this work, to ensure that the comparison with DFM is not complicated by the (minor) effects of the truncation.

[27] The solution is obtained by making the tractions (18) on the interface agree with the jump conditions (3)–(4) that involve the frictional strength (5)–(6). The shear traction vector $\boldsymbol{\tau}$ and the compressive normal stress σ_n that enter (3)–(6) are given in terms of tractions $\tau_\nu(x, y, t)$ by

$$\boldsymbol{\tau} = (\tau_x, \tau_y); \quad \tau = \sqrt{\tau_x^2 + \tau_y^2}; \quad \sigma_n = \tau_z. \tag{24}$$

The details of the solution procedure are given in Appendix B.

5. Test Problem

[28] Our numerical test entails solving the spontaneous rupture problem for a planar fault embedded in a uniform infinite elastic isotropic space. The formulation and parameters of the test case correspond to Version 3 of the Southern California Earthquake Center (SCEC) benchmark problem developed for the second SCEC Spontaneous Rupture Code-Validation Workshop of 2004 [*Harris et al.*, 2004]. The problem geometry is shown in Figure 2. This test problem, because it is restricted to a uniform unbounded elastic medium, can be solved by the BI method, as well as by the DFM method (with a sufficiently large grid to avoid spurious boundary reflections). We take the fault plane to be the xy plane. The shear prestress is aligned with the x axis, and the origin of the coordinate system is located in the middle of the fault, as shown in Figure 2. The fault and prestress geometries are such that the x and y axes are axes of symmetry (or antisymmetry) for the fault slip and traction components. As a result, the xz plane undergoes purely in-plane motion, and the yz plane purely antiplane motion.

[29] Rupture is allowed within a fault area 30 km in the x direction and 15 km in the y direction. A homogeneous medium is assumed, with a P wave velocity of 6 km/s, S wave velocity of 3464 m/s, and density of 2670 kg/m^3. The distributions of the initial stresses and frictional parameters on the fault are specified in Table 1. The nucleation occurs in 3 km $\times$ 3 km square area that is centered on the fault, as shown in Figure 2. The rupture initiates because the initial shear stress in the nucleation patch is set to be slightly (0.44%) higher than the initial static yield stress in that patch. Then the rupture propagates spontaneously through the fault area, following the linear slip-weakening fracture criterion (5)–(6). The rupture cannot propagate beyond the 30 km $\times$ 15 km region due to the high static frictional strength set outside the region, and the region boundaries send arrest waves that ultimately stop the rupture. The duration of the simulation until the full arrest of the slip is about 12 s.

[30] We computed seven DFM solutions and eight BI solutions to the test problem, with grid intervals and time steps shown in Table 2. All DFM solutions use a uniform, cubic mesh. Grid intervals for the DFM solutions range from 0.05 km to 0.3 km. The smallest grid interval was Δx = 0.05 km (with time step 0.005 s), and the corresponding solution is denoted DFM0.05. The other DFM solutions are given similar designations, for example, the case Δx = 0.1 km (with time step 0.008) is denoted DFM0.1. BI solutions use grid sizes Δx ranging from 0.1 km (with time step 0.00962 s) to 0.75 km, with a naming convention analogous to that used for the DFM solutions. Although our principal objective is to compare the DFM and BI solutions, comparison of the various DFM (or BI) solutions with each other is also informative, in that it helps establish the degree to which grid size invariance has been achieved in the numerical solutions. The DFM and BI calculations were done independently, initially as a part of a blind test of

Table 1. Stress and Frictional Parameters for Test Problem

Parameters	Within Fault Area of 30 km × 15 km		Outside Fault Area
	Nucleation	Outside Nucleation	
Initial shear stress τ_0, MPa	81.6	70.0	70.0
Initial normal stress $-\sigma_n$, MPa	120.0	120.0	120.0
Static friction coefficient μ_s	0.677	0.677	infinite
Dynamic friction coefficient μ_d	0.525	0.525	0.525
Static yielding stress $\tau_s = -\mu_s\sigma_n$, MPa	81.24	81.24	infinite
Dynamic yielding stress $\tau_d = -\mu_d\sigma_n$, MPa	63.0	63.0	63.0
Dynamic stress drop $\Delta\tau = \tau_0 - \tau_d$, MPa	18.6	7.0	7.0
Strength excess $\tau_s - \tau_0$, MPa	−0.36	11.24	infinite
Critical slip distance d_0, m	0.40	0.40	0.40

Table 2. Test Problem Calculations

Calculation Name	Solution Method	Spatial Step Δx, km	Time Step Δt, s	Median Resolution $\bar{N}_c$	Minimum Resolution $N_c^{\min}$
BI0.1	BI	0.1	0.00962	4.4	3.3
BI0.15	BI	0.15	0.01443	2.9	2.2
BI0.2	BI	0.2	0.01924	2.2	1.6
BI0.25	BI	0.25	0.02406	1.7	1.3
BI0.3	BI	0.3	0.02887	1.5	1.1
BI0.5	BI	0.5	0.04811	0.9	0.65
BI0.6	BI	0.6	0.05774	0.7	0.54
BI0.75	BI	0.75	0.07217	0.6	0.43
DFM0.05	DFM	0.05	0.005	8.7	6.5
DFM0.075	DFM	0.075	0.00625	5.8	4.3
DFM0.1	DFM	0.1	0.008	4.4	3.3
DFM0.15	DFM	0.15	0.0125	2.9	2.2
DFM0.2	DFM	0.2	0.016	2.2	1.6
DFM0.25	DFM	0.25	0.015	1.7	1.3
DFM0.3	DFM	0.3	0.020	1.5	1.1

spontaneous rupture algorithms coordinated by SCEC [*Harris et al.*, 2004].

6. Cohesive Zone and Constraints on Discretization

[31] An important dimensionless measure of the resolution of numerical methods is the ratio N_c of the size (also called width or length) Λ of the cohesive (or slip weakening) zone to the grid spacing Δx, i.e., the number of fault plane node points (measured in the direction of rupture propagation) defining the cohesive zone:

$$N_c = \Lambda/\Delta x. \tag{25}$$

The cohesive zone is the portion of the fault plane behind the crack tip where the shear stress decreases from its static value to its dynamic value and slip path length ℓ satisfies $0 < \ell < d_0$ [e.g., *Ida*, 1972]. In the cohesive zone, shear stress and slip rate vary significantly, and proper numerical resolution of those changes is crucial for capturing the maximum slip rates and the rupture propagation speeds.

[32] Here we review some concepts of linear fracture mechanics and simple estimates for the cohesive zone size in two-dimensional cases of mode II and mode III, following and combining results by *Palmer and Rice* [1973] *Andrews* [1976, 2004], *Rice* [1980], and *Freund* [1989]. Note that while the rupture considered here is three-dimensional, it proceeds in mode II or in-plane mode along the x axis and in mode III or antiplane mode along the y axis of the fault plane. Following standard treatment in fracture mechanics, we consider a planar semi-infinite crack with constant shear traction $\tau_d = -\sigma_n \mu_d$ everywhere on the crack surfaces except for the cohesive zone $0 < \xi < \Lambda$ behind the crack tip (given by $\xi = 0$), where the shear traction $\tau(\xi)$ varies from the peak shear stress $\tau_s = -\sigma_n \mu_s$ to τ_d. While our crack is not semi-infinite, this is a good approximation for the region near the crack tip. Let us assume that the cohesive zone width is small enough relative to the overall rupture size that we can employ the small-scale yielding limit of fracture mechanics [*Rice*, 1968]. In that limit, the stress field that surrounds the cohesive zone is assumed to be dominated by the singular part of the crack field, characterized by the stress intensity factor K, which is either K_{II} for mode II or K_{III} for mode III. Finally, we consider the crack propagation to be steady, with the constant crack (or rupture) speed υ. The results obtained with the assumptions of steady rupture should still be reasonably accurate for the unsteady case, provided that the crack speed does not change significantly over propagation distances comparable to the cohesive zone length or several times that [*Freund*, 1989]. In the following, we use subscripts II or III to indicate that the quantity is related to mode II or III; the same quantities with no subscript participate in expressions valid for both mode II and III.

[33] The balance of the energy release rate G and fracture energy Γ at the crack tip can be written as [e.g., *Freund*, 1989]

$$G \equiv A(\upsilon) K^2/(2\mu^*) = \Gamma, \tag{26}$$

where $\mu^*_{\mathrm{III}} = \mu$, $\mu^*_{\mathrm{II}} = \mu/(1-\nu)$, μ is the shear modulus, ν is the Poisson's ratio, Γ is the fracture energy, and functions $A(\upsilon)$ are known dimensionless functions of crack tip speed υ [i.e., *Freund*, 1989]. The fracture energy Γ is given by the cohesive zone law; in our case,

$$\Gamma = d_o(\tau_s - \tau_d)/2. \tag{27}$$

Since the cohesive zone presence eliminates the singularity at the crack tip, K and $\tau(\xi)$ must be related by [e.g., *Rice*, 1980; *Freund*, 1989]

$$K = \sqrt{\frac{2}{\pi}} \int_0^{\Lambda} \frac{\tau(\xi) - \tau_d}{\sqrt{\xi}} d\xi. \tag{28}$$

[34] A useful estimate of the cohesive zone size can be derived from (26)–(28) if we assume that the traction distribution within the cohesive zone is a function only of ξ/Λ, i.e.,

$$\tau(\xi) = \tau_s - (\tau_s - \tau_d) f(\xi/\Lambda), \;\; f(0) = 0, \;\; f(1) = 1. \tag{29a}$$

Then from (28), the cohesive zone width Λ can be expressed as

$$\Lambda = C_1 \frac{K^2}{(\tau_s - \tau_d)^2}, \quad C_1 = \sqrt{\frac{2}{\pi}} \int_0^1 \frac{1 - f(\varsigma)}{\sqrt{\varsigma}} d\varsigma. \tag{29b}$$

To estimate the constant C_1, we assume that the traction distribution within the cohesive zone is linear, i.e., $\tau(\xi) = \tau_s - (\tau_s - \tau_d)\xi/\Lambda$, in which case $C_1 = 9\pi/32$. Note that our cohesive relation comes from friction laws (5)–(6), and the shear tractions are given as a linear function of slip-path length ℓ, not space variable ξ. However, simulations show that this is a good assumption, as shear tractions within the cohesive zone are approximately linear with ξ. Determining K^2 from (26)–(27) and substituting into (29b), we obtain

$$\Lambda = \Lambda_o A^{-1}(\upsilon), \quad \Lambda_o = C_1 \frac{\mu^* d_o}{(\tau_s - \tau_d)}, \tag{30a}$$

where

$$\mu^*_{\mathrm{III}} = \mu,\ \mu^*_{\mathrm{II}} = \mu/(1-\nu);\ A^{-1}_{\mathrm{III}} = \left(1 - \upsilon^2/\beta^2\right)^{1/2},$$
$$A^{-1}_{\mathrm{II}} = \frac{(1-\nu)\beta^2\mathcal{D}}{\upsilon^2\left(1-\upsilon^2/\beta^2\right)^{1/2}},$$
$$\mathcal{D} = 4\left(1-\upsilon^2/\beta^2\right)^{1/2}\left(1-\upsilon^2/\beta^2\right)^{1/2} - \left(2-\ \upsilon^2/\beta^2\right)^2;$$
$$C_1 = 9\pi/32 \text{ for linear } \tau(\xi). \tag{30b}$$

In (30a), since A^{-1} (0^+) = 1, Λ_o denotes the cohesive zone size that the crack has when its speed is $\upsilon = 0^+$ (the crack is barely moving). $A^{-1}(\upsilon)$ are decreasing functions of the rupture speed v, and $A^{-1}(\upsilon) \to 0$ as $\upsilon \to c_R$ (Rayleigh wave speed) for mode II or $\upsilon \to \beta$ (shear wave speed) for mode III. Hence we see that as the crack velocity increases, the cohesive zone undergoes Lorentz contraction in the direction of rupture propagation, its width collapsing as A^{-1} (υ) given in (30b).

[35] Λ_o provides a convenient upper bound for the cohesive zone size (it is an upper bound in the sense that any nonzero rupture speed would shrink this zone even further as predicted by (30a)). The expression for Λ_o with $C_1 = 9\pi/32$ was originally derived by *Palmer and Rice* [1973] and then discussed by *Rice* [1980]. In numerical simulations, one should definitely resolve Λ_o with more than one spatial element, as we discuss further at the end of this section.

[36] To come up with an estimate for the cohesive zone size Λ that accounts also for the effect of rupture speeds and their change with the propagation distance, we need to make some reasonable assumptions about the development of the stress intensity factor K as the rupture propagates. We can then use (26) to estimate the rupture speeds υ, and corresponding contraction factor $A^{-1}(\upsilon)$, that would result from such K. Under a wide range of conditions [e.g., *Freund*, 1989; *Broberg*, 1999], K can be factored as

$$K = k(\upsilon)K^{ref}, \tag{31}$$

where $k(\upsilon)$ are known dimensionless functions of the rupture speed and K^{ref} is the equilibrium stress intensity factor that depends on the given applied loading and characteristic crack dimension but is independent of the rupture speed. Note that (31) is derived for a semi-infinite crack propagating in an infinite medium and does not account for effects of boundaries or finite crack size. For example, in the case of a finite crack, the stress field of the opposite crack tip influences K, so its precise value depends upon the past history of rupture. We neglect this memory and other potential effects, and consider the case in which K^{ref} is only determined by stress released on the fault, given by the stress drop $\Delta\tau = \tau_o - \tau_d$, and the length of the rupture $2L$. The dimensional considerations dictate the form

$$K^{\mathrm{ref}} = C_2 L^{1/2}\Delta\tau, \tag{32}$$

where C_2 is a constant of order 1. For the case of a static mode II or mode III crack of length $2L$ embedded in an infinite elastic medium, $C_2 = \sqrt{\pi}$.

[37] Now we can substitute the assumed stress intensity factor (31)–(32) into the crack tip energy balance (26)–(27) and then solve the resulting equation for the crack speed υ and hence the Lorentz contraction factor $A^{-1}(\upsilon)$. This is possible to do analytically only for the mode III case. The result is

$$A^{-1}_{\mathrm{III}}(\upsilon) = \left(1-\upsilon^2/\beta^2\right)^{1/2} = \frac{2L_0/L}{1+(L_0/L)^2}, \tag{33}$$

where $2L_o$ is the size of the crack when $\upsilon = 0^+$ or $2L_o$ is the critical crack length, given by

$$L_0 = \frac{\mu d_0(\tau_s - \tau_d)}{C_2^2(\tau_o - \tau_d)^2} = \frac{\mu d_0(S+1)}{C_2^2\Delta\tau}. \tag{34}$$

In (34), $S = (\tau_s - \tau_o)/\Delta\tau$ is the dimensionless strength parameter [*Das and Aki*, 1977], $\Delta\tau = \tau_o - \tau_d$, and, for a static mode II or mode III crack, $C_2^2 = \pi$. For the parameters of the test problem, $2L_o \approx 3$ km which motivates the 3-km choice for nucleation region size in the test problem. Note that the nucleation region is overstressed which ensures that slip there starts right away.

[38] We can combine these results in two ways. First, substituting the Lorentz factor (33) into the cohesive zone expression (30), we obtain

$$\Lambda = \Lambda_o \frac{2L_0/L}{1+(L_0/L)^2}, \tag{35}$$

which shows how the zero-speed cohesive zone size Λ_o decreases as the rupture lengthens (or propagates). Additionally, by writing out explicitly Λ_o and L_0 in the numerator of (35), we get

$$\Lambda = \frac{C_1}{C_2^2}\left(\frac{\mu d_0}{\Delta\tau}\right)^2\left(\frac{1}{1+L_0^2/L^2}\right)L^{-1}. \tag{36}$$

In (36), the only dependence upon the relative strength factor S is contained in the critical crack half-length L_0. For crack sizes L large compared to the critical crack size L_0, we get

$$\Lambda = \frac{C_1}{C_2^2}\left(\frac{\mu d_0}{\Delta\tau}\right)^2 L^{-1}, \quad L \gg L_o, \tag{37}$$

where on the basis of the values of C_1 and C_2 introduced above, $C_1/C_2^2 = 9/16$. Note that under the assumptions made, the cohesive zone size Λ is independent of $(\tau_s - \tau_d)$ and hence, for a given $\Delta\tau$, of the relative strength factor S. Physically, the absence of strong dependence on $(\tau_s - \tau_d)$ arises from the following trade-off: reducing $(\tau_s - \tau_d)$ increases the zero-speed cohesive zone length Λ_o (equation (30)), but it also increases the rupture velocity occurring at a given rupture distance L, producing a compensating Lorentz contraction (equations (33) and (34)). Note also that the cohesive zone size is inversely proportional to the crack half-length L. For $L \gg L_o$, the crack half-length L would be approximately equal to the propagation distance. The functional form (37) is identical to

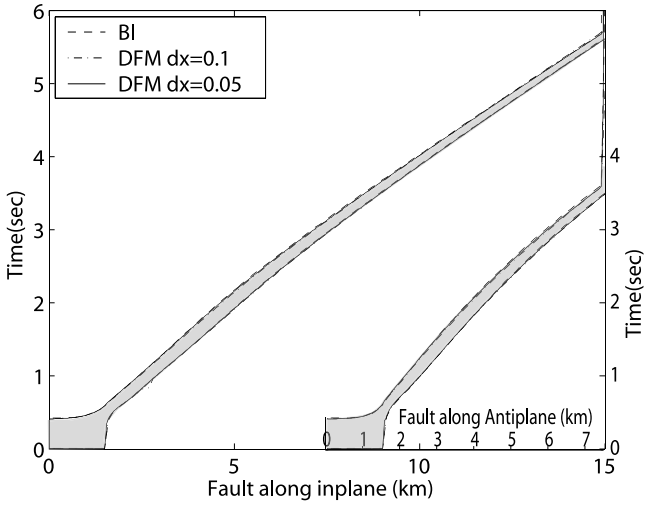

Figure 3. Cohesive zone during rupture, along both in-plane and antiplane directions for BI0.1 (dashed curve), DFM0.1 (dash-dotted curve), and DFM0.05 (solid curve) solutions.

Andrews' [1976, 2004, 2005] estimate obtained by somewhat different considerations.

[39] Hence we have at least two ways to estimate the cohesive zone size and calibrate numerical resolution: the zero-speed cohesive zone size Λ_o given by (30) and the approximate solution (37) for Λ at large propagation distances. The two estimates are complementary. The Λ_o estimate shows that regardless of the background stress or rupture propagation distances, the numerical resolution is already constrained by the choice of the frictional parameters and elastic bulk properties. For the parameters used in our test problem and $C_1 = 9\pi/32$, we find

$$\Lambda_{\mathrm{III}o} = 620 \text{ m}, \quad \Lambda_{\mathrm{II}o} = 827 \text{ m}, \tag{38}$$

where $\Lambda_{\mathrm{II}o}$ and $\Lambda_{\mathrm{III}o}$ refer to the values for mode II and mode III, respectively. Since we need several spatial nodes within Λ_o to accommodate the Lorentz contraction, these estimates already indicate that good spatial resolution of our problem would involve grid sizes of order 100 m or smaller. The Λ estimate attempts to incorporate the background stress level (through the stress drop $\Delta\tau$) and the reduction of the cohesive zone due to the increasing crack speed v for large propagation distances L. Using expression (37) with the maximum antiplane propagation distance $L = 7.5$ km and $C_1/C_2^2 = 9/16$, we obtain

$$\Lambda^{\mathrm{est}}_{\mathrm{IIImin}} = 251 \text{ m}. \tag{39a}$$

For mode II, we cannot derive an analytical formula like (37), but we can perform the procedure numerically. For a given L, we compute K from (31)–(32) and substitute it into the crack tip balance (26). This results in an equation with respect to the crack speed v which can be solved numerically. Then we use that v to find Λ from (30a). Taking $L = 15$ km, the largest propagation distance in the in-plane direction, we get

$$\Lambda^{\mathrm{est}}_{\mathrm{IImin}} = 190 \text{ m}. \tag{39b}$$

[40] Both the Λ_o estimate from (30) and the Λ estimate (37) should give good initial guidance as to what kind of spatial resolution will be needed in dynamic rupture propagation problems. However, one should not expect a perfect quantitative agreement, as the estimates are derived with a number of simplifying assumptions. For example, we use the small-scale yielding assumption, the validity of which in any real situation would be only approximate. In addition, the most uncertain part of the Λ estimate is the set of assumptions made about the stress intensity factor. Finally, crack problems usually have features not considered in this analysis. For example, our test problem is three-dimensional, and the crack is initiated rather abruptly, by overstressing a region in the middle of the fault, which would certainly affect its development.

[41] Still, both estimates (38) and (39) compare very well, in the qualitative sense, with the actual results of our computation. Figure 3 shows the cohesive zone development in both antiplane and in-plane directions. For measuring Λ, we define the leading edge of the cohesive zone as the spatial grid point at which the shear traction reaches τ_s, and include in the cohesive zone the interval over which the shear traction decreases to τ_d. The comparison between the estimates and the observed values makes sense only well outside the nucleation zone, which is artificially overstressed ($\tau_o > \tau_s$). We see that right outside the nucleation zone, the cohesive zone abruptly narrows and then starts to expand. These features are clearly due to the overstressed nucleation. The smallest size of the cohesive zone right after nucleation is 300 m and it is in the antiplane direction (all values reported in this section are based on the BI0.1 solution). Some time later the maximum sizes $\Lambda_{\mathrm{IIImax}}$ in the antiplane direction and Λ_{IImax} in the in-plane direction are reached:

$$\Lambda_{\mathrm{IIImax}} = 460 \text{ m}, \quad \Lambda_{\mathrm{IImax}} = 560 \text{ m}. \tag{40}$$

After these nucleation-dominated effects, the cohesive zone progressively decreases, consistently with the theoretical developments above, reaching its subsequent smallest values at the ends of the fault:

$$\Lambda_{\mathrm{IIImin}} = 350 \text{ m}, \quad \Lambda_{\mathrm{IImin}} = 325 \text{ m}. \tag{41}$$

Hence we see that the Λ_o estimate (38) gives a very close upper bound to all cohesive zone sizes observed in our simulation. Moreover, the BI simulation with the spatial resolution $\Delta x = 1$ km, which is just slightly larger than both $\Lambda_{\mathrm{III}o} = 620$ m and $\Lambda_{\mathrm{II}o} = 827$ m, results in very oscillatory behavior that makes the rupture arrest right after leaving the nucleation patch (that is why we do not include this run in our comparison and Table 2) while the BI simulation with $\Delta x = 0.75$ km, which resolves Λ_o with about one cell size, still results in the rupture spreading throughout the fault, even though the results are not very accurate compared with our best resolved and convergent solutions. Hence resolving Λ_o is absolutely critical, and of course more than one cell is required for good results as discussed in the next section. Notice also that $\Lambda_{\mathrm{III}o}/\Lambda\mathrm{I}_o = 3/4 = 1/(1-\nu)$ (where $\nu = 0.25$ is the Poisson's ratio), which predicts that for the same propagation distances, the cohesive zone sizes in the

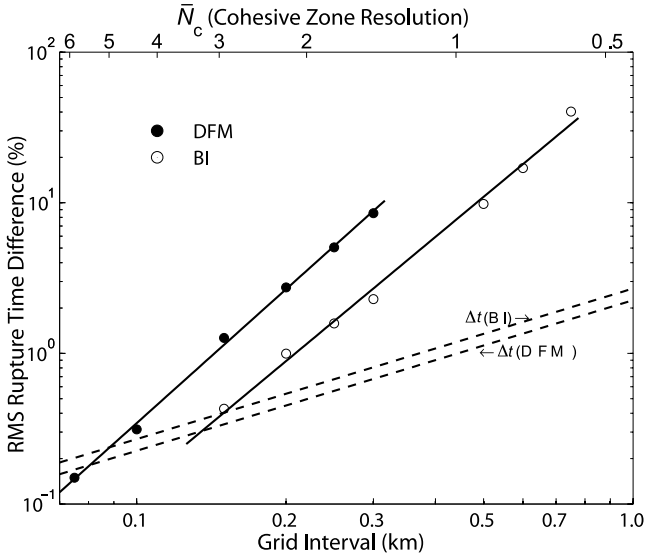

Figure 4. Differences in time of rupture, relative to reference solution, shown as a function of grid interval Δx. Differences are RMS averages over the fault plane. Solid circles are DFM solutions, relative to DFM0.05 (the smallest grid interval DFM case). Open circles are BI solutions, relative to BI0.1 (the smallest grid interval BI case). The dashed lines show the (approximate) dependence of time step Δt on Δx. The top axis characterizes the calculations by their characteristic $\bar{N}_c$ values, where $\bar{N}_c$ is median cohesive zone width in the in-plane direction divided by Δx. Note the power law convergence of both methods as the grid size is reduced. The 90% confidence intervals on the power law exponents suggested by the regression lines are DFM [2.77–3.15] and BI [2.44–3.04], indicating approximately equal convergence rates for the two methods.

antiplane direction should be smaller than the cohesive zone sizes in the in-plane direction, exactly what we observe. However, the in-plane direction has a longer extent and ultimately results in a smaller cohesive zone at the end of the fault, as values (41) show. This is predicted by the estimates of $\Lambda_{\min}$ given in (39). The estimates of $\Lambda_{\min}$ are smaller than the actual values by a factor of about 1.5 (which is a constant of order 1), which we consider a very good qualitative agreement.

[42] We conclude that one can use estimates (30) and (37) very effectively to approximately determine cohesive zone sizes that would occur in a spontaneous rupture simulation. As we describe further in the following sections, proper resolution of the cohesive zone sizes is crucial for obtaining convergent numerical results.

[43] To quantify our resolution, we need to report the number of spatial elements or grid points we have within the cohesive zone, given by the parameter $N_c = \Lambda/\Delta x$ defined in (25). However, the cohesive zone size changes as the crack propagates, and hence N_c is not a single number but rather a variable quantity. In the next section, where we calculate some global metrics of the numerical solutions to characterize their differences, it will be convenient to have a corresponding index characterizing globally the level of cohesive zone resolution attained in a given numerical solution. Hence we define a resolution index $\bar{N}_c$ based on the median value of N_c obtained in the BI0.1 solution in the in-plane direction (because the in-plane direction is longer and hence likely to be representative of more points on the fault). We will also report $N_c^{\min}$, the minimum of N_c in the in-plane direction, as that value represents the worst local resolution achieved. Taking the spatial values in km consistently with the definition of grid sizes in Table 2, we get

$$\overline{N}_c = \overline{\Lambda}_{\mathrm{II}}/\Delta x, \quad N_c^{\min} = \Lambda_{\mathrm{IImin}}/\Delta x, \tag{42}$$

where $\overline{\Lambda}_{\mathrm{II}} = 0.44$ km and $\Lambda_{\mathrm{IImin}} = 0.33$ km are, respectively, the median and minimum cohesive zone sizes we observe in our simulations in the in-plane direction. Values of $\overline{N}_c$ and $N_c^{\min}$ are reported in Table 2.

7. Comparison of Numerical Results

[44] We compare results in two stages. First, we quantify the differences in the DFM and BI solutions, respectively, as the grid interval Δx is varied. Then we focus on quantitative and qualitative comparisons of three relatively high-resolution solutions, DFM0.05, DFM0.1, and BI0.1.

7.1. Grid Dependence of Solutions

[45] For the spontaneous rupture problem, the rupture arrival time (referred to as "rupture time" in the following) is a rather sensitive indicator of numerical precision. This sensitivity reflects the nonlinearity of the problem: Since rupture can only occur after the shear stress reaches a threshold value, relatively small inaccuracies in the calculated stress field can be expected to very significantly affect the timing of rupture breakout from the nucleation zone as well as the subsequent rupture velocity. If the rupture times are captured well, so is the rupture tip speed (or crack speed), and the rupture speed is one of the factors that influence seismic signals most. Plus, higher rupture speeds are linked to higher maximum slip rates, and hence accurate rupture times mean that the slip rates are also captured reasonably well. Therefore we have used rupture time differences as a primary means to quantify differences between solutions, with rupture time of a point on the interface defined here as the time at which the slip rate at that point first exceeds 1.0 mm/s.

[46] The rupture time comparisons are summarized in Figure 4. Note that the abscissa is denoted in two different ways on Figure 4. On the bottom, the grid size is given. On the top, we show the corresponding median cohesive zone resolution parameter $\overline{N}_c$ given by (42).

[47] Using DFM0.05 as a reference, solid circles in Figure 4 show rupture time difference as a function of grid interval for the DFM calculations. The quantity plotted is the root mean square (RMS) difference of rupture times relative to DFM0.05, with the average taken over all fault plane nodes outside the nucleation patch; the result is then expressed as a percentage of the mean rupture time in DFM0.05. The RMS differences for DFM calculations appear to follow a power law in the grid size, with estimated exponent 2.96 (90% confidence interval 2.77 to 3.15). The dashed lines in Figure 4 show the numerical time step sizes as a function of Δx. The rupture time difference between

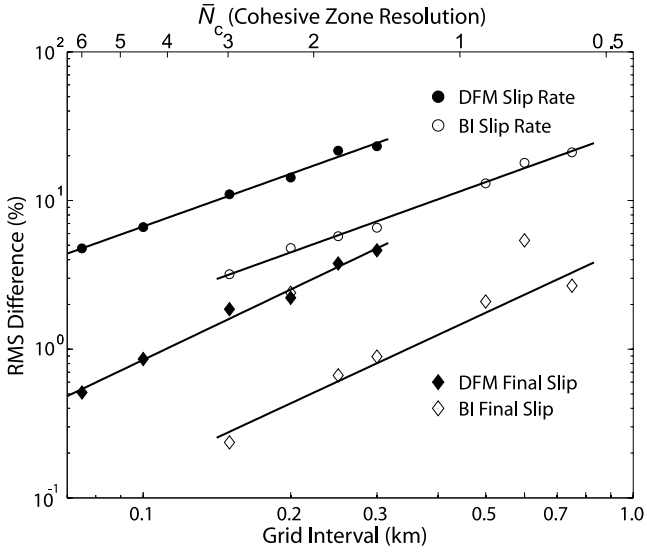

Figure 5. Differences in final slip (diamonds) and peak slip velocity (circles), relative to reference solution, shown as a function of grid interval Δx. Differences are RMS averages over the x and y axes of the fault plane. Solid symbols are DFM solutions, relative to DFM0.05 (the smallest grid interval DFM case). Open symbols are BI solutions, relative to BI0.1 (the smallest grid interval BI case). Note the power law convergence of both methods as the grid size is reduced. The 90% confidence intervals on the power law exponents suggested by the regression lines are: DFM displacement [1.31–1.84]; BI displacement [1.07–1.99]; DFM velocity [1.02–1.33]; BI velocity [1.04–1.33]. Outliers at Δx = 0.2 km and 0.6 km were not used in estimating the BI displacement slope (see discussion in text).

DFM0.1 and DFM0.05 closely approaches (within 20%) the one time step threshold, and the time difference between DFM0.075 and DFM0.05 falls below that. Thus we conclude that the DFM solution has achieved rupture time stability, to within about one time step, for $\Delta x \leq 0.1$ km, corresponding to $\overline{N}_c \geq 4.4$ ($N_c^{\min} \geq 3.3$).

[48] Open circles in Figure 4 show the rupture time differences for BI, using BI0.1 as a reference. As for DFM, the rupture time differences exhibit power law behavior in the grid size. The slope, 2.74 (90% confidence interval 2.44 to 3.04), is not significantly different from that for the DFM case. The BI solution achieves rupture time stability to within about a time step with $\Delta x \leq 0.15$ km, corresponding to $\overline{N}_c \geq 2.9$ ($N_c^{\min} \geq 2.2$), which is an $\overline{N}_c$ value about 2/3 the DFM requirement (i.e., BI achieves the same convergence with 50% larger Δx than DFM).

[49] Figure 5 summarizes the behaviors of two additional measures of grid size dependence: final slip and maximum slip velocity. Each diamond (solid for DFM, open for BI) represents an RMS average (taken over the points along the x and y axes) of the difference in final slip between the solution for a given Δx value and a reference solution. The circles are the corresponding RMS averages for peak slip velocity. As before, DFM0.05 serves as the reference for all the DFM calculations, and BI0.1 serves as the reference for all the BI calculations. As was the case for the rupture times, the slip and slip velocity differences have roughly power law behavior, with exponents between 1 and 2. The displacement differences have steeper slopes than the peak velocity slopes, but 90% confidence intervals for the slopes overlap. The peak slip velocity difference falls to ~7% or less for $\Delta x \leq 0.1$ km ($\overline{N}_c \geq 4.4$) for DFM, and for $\Delta x \leq 0.3$ km ($\overline{N}_c \geq 1.5$) for BI. Similarly, the final slip difference falls to ~1% or below for $\Delta x \leq 0.1$ km ($\overline{N}_c \geq 4.4$) for DFM, and for $\Delta x \leq 0.3$ km ($\overline{N}_c \geq 1.5$) for BI. The BI peak slip velocities and final slips converge to within a given tolerance level with $\overline{N}_c$ about 1/3 the DFM requirement for the same tolerance level.

[50] Note that BI slip comparisons in Figure 5 (open diamonds) contain two outliers, the computations with Δx = 0.2 km and Δx = 0.6 km. These runs have larger discrepancies in final slip because the simulated domain in these runs is slightly asymmetric with respect to the central nucleation zone. Consider the case with Δx = 0.2 km. The nucleation region (which is 3 km × 3 km) has 15 cells in the x direction, an odd number, while the fault domain (which is 30 km × 15 km) has 150 cells in the x direction, an even number. Hence, in the x direction, there have to be different numbers of cells to the left and to the right of the nucleation zone (Figure 2); we choose 62 cells to the left and 63 cells to the right. This makes the nucleation zone slightly asymmetric with respect to the fault boundaries and the geometry slightly different from the runs that simulate the original symmetric problem. The slight asymmetry does not affect the rupture times and peak velocities, as these are reached before the rupture samples the boundaries of the fault zone, but the final slips depend on the arrest waves from the boundaries and are affected.

[51] In our calculations, the time step is proportional to the grid size, as reflected by the dashed lines of Figure 4, and hence the resolution can be characterized by the grid spacing Δx only, or by N_c as its nondimensional measure. However, the BI calculation for a given Δx can be somewhat improved by taking smaller time steps. We do not attempt to quantify this here, but note that as a result, for a different proportionality factor between the grid size and the time step, or for a case where lower spatial resolutions use smaller time steps, the convergence rates could be somewhat different, and hence adequate performance could be reached for slightly larger Δx (or smaller N_c).

[52] We conclude that both DFM and BI solutions have achieved numerical convergence with respect to grid size reduction. Notably, the BI and DFM methods appear to have the same convergence rates, as indicated by the near equality of the corresponding DFM and BI slopes in Figures 4 and 5. Note, however, that for each measure (rupture time, peak slip velocity, final slip), BI solutions, for a given Δx, have smaller differences with the BI best resolved solution, BI0.1, than the corresponding DFM solutions have with their best resolved solution, DFM0.05. For rupture time, BI achieves the given tolerance level for $\overline{N}_c$ about a factor of 1.5 lower than DFM; for peak slip velocity and final slip, BI achieves the given tolerance level for $\overline{N}_c$ about a factor of 3 lower than DFM.

7.2. Comparison of High-Resolution Solutions

[53] Three relatively high-resolution solutions of the test problem are compared in Figures 6 to 9. For this purpose,

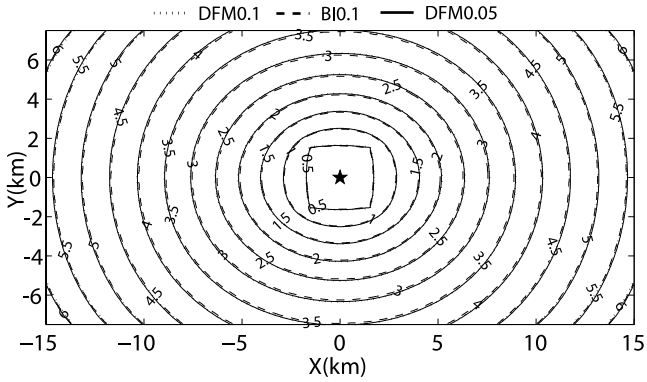

Figure 6. Contour plot of the rupture front for the dynamic rupture test problem. Solid curves are for DFM0.05 (grid size Δx = 0.05 km); dotted curves are for DFM0.1 (grid size Δx = 0.1 km); dashed curves are for BI0.1 (grid size Δx = 0.1 km).

we use the highest-resolution solution for each method (DFM0.05 and BI0.1, respectively), and also include DFM0.1 to provide a direct comparison between the two methods when the same grid interval is employed. Recall that DFM0.1 and BI0.1 represent the cohesive zone with $\overline{N}_c$ of 4.4 node points (and $N_c^{\min}$ = 3.3), and that DFM0.05 represents the cohesive zone with $\overline{N}_c$ of 8.7 node points (and $N_c^{\min}$ = 6.5).

[54] Figure 6 shows contours of rupture time for these three solutions. The computed evolution of the rupture front is virtually identical for all three solutions. The level of agreement appears to be good at all distances, from the nucleation patch to the outer edge of the rupture surface, and even details such as the sharp corners of the 0.5 s contour, as the rupture breaks out of the nucleation patch, are virtually indistinguishable in the three solutions. The maximum difference in rupture time between DFM0.1 and BI0.1 is 0.055 s, and the RMS value (averaging over the fault plane) of the difference is 0.028 s. On the basis of the average rupture time on the fault of 3.57 s, this RMS difference is about 0.8%. The maximum and RMS differences between DFM0.05 and BI0.1 are 0.045 s (1.3%) and 0.027 s (0.8%), respectively. The maximum and RMS differences between DFM0.05 and DFM0.1 are 0.046 s (1.3%) and 0.011 s (0.3%), respectively (see Table 3).

[55] Table 3 gives the maximum and RMS values of the differences in peak velocity and final slip between DFM and BI solutions. The RMS differences between BI0.1 and DFM0.05 are less than 3% in peak slip velocity, and less than 0.5% in final slip.

[56] Figure 7 shows the time histories at the two fault plane points marked in Figure 2, one each on the in-plane (point PI) and antiplane (point PA) axes, respectively. The time histories presented are the direct result of our simulations, with no additional filtering of any kind. In each case, the shear stress time histories are nearly identical among the three solutions. Arrival times of rupture and several identifiable stopping phases are nearly indistinguishable in the three solutions, as are the times of arrest of sliding. Even occurrence, timing, and duration of the small reactivation of slip, at ~8 s at PI and at ~10.3 s at PA, are nearly identical in the three solutions. Note particularly that at the in-plane site, both the initial stress increase associated with the P wave (arriving at ~1.5 s), and the subsequent shear decrease associated with the S wave (arriving at ~2.2 s) are replicated to high precision. Likewise, at the antiplane site, the small stress decrease associated with the near-field P wave is modeled nearly identically by the three solutions. The displacement curves also agree very closely in all cases.

[57] The only notable discrepancy is for slip velocity at PA. Even at this location, DFM0.05 and BI0.1 agree quite well. However, DFM0.1 oscillates about DFM0.05 and BI0.1, with fluctuation amplitude of about 15% of the peak velocity at the onset of motion, decaying rapidly to amplitude less than 1% of peak velocity. BI0.1 and DFM0.05 are nearly free of oscillations. The region near PA is representative of the worst case for DFM0.1 with respect to these rupture front velocity fluctuations, which is consistent with the fact that in that region, the cohesive zone has contracted to near its minimum (due to postnucleation effects), with the local N_c only ~3.5 for DFM0.1, and ~7 for DFM0.05 (see Figure 3). At the PI site, where the cohesive zone width corresponds to N_c ~5 for DFM0.1 (and to ~10 for DFM0.05) any velocity oscillations in DFM0.1 are at least an order of magnitude smaller: the two DFM solutions are smooth and virtually identical. All of these observations are consistent with a criterion of $N_c \geq \sim 5$ for obtaining slip velocity estimates accurate to a few percent in DFM solutions, provided this criterion is satisfied locally, however, and not just in an average sense. For BI solutions, the slip velocities for BI0.1 are nearly oscillation free, which confirms the rupture time result that $N_c \geq \sim 3$ is sufficient resolution for BI.

[58] Slip rate and shear stress time history profiles along the x axis (in-plane direction) (Figure 8) and the y axis

Table 3. Misfit Measures for the Three Pairs of High-Resolution Solutions

	DFM0.05 Versus DFM0.1	DFM0.1 Versus BI0.1	DFM0.05 Versus BI0.1
	Rupture Arrival Time		
Maximum difference,%	1.29	1.53	1.26
RMS,%	0.31	0.78	0.76
	Final Slip (Along the x and y Axes)		
Maximum difference,%	3.0	1.42	2.07
RMS,%	0.86	0.64	0.44
	Peak Slip Velocity (Along the x and y Axes)		
Maximum difference,%	18.1	38.7	21.9
RMS,%	6.6	8.9	3.0

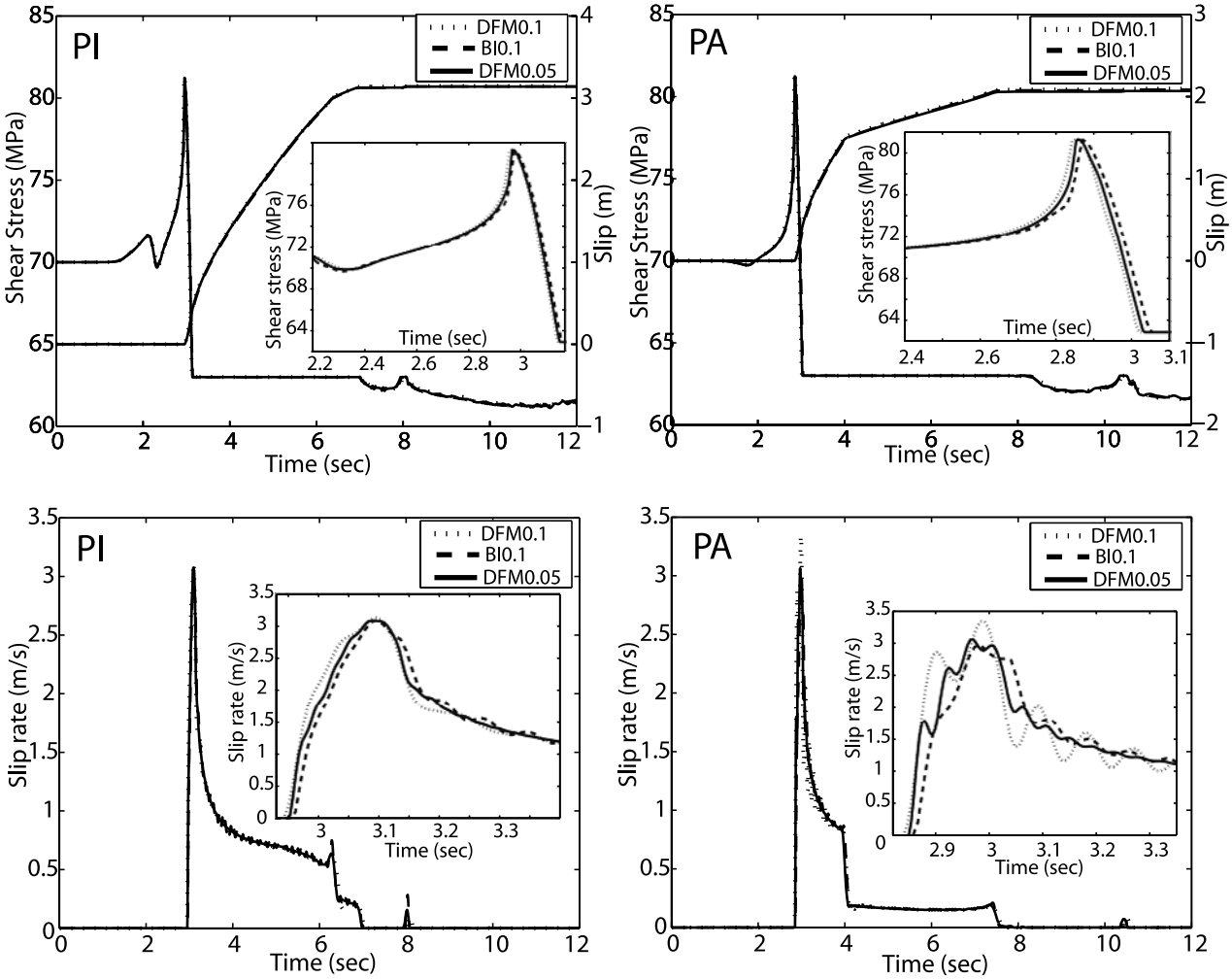

Figure 7. Time histories at the two fault plane points marked in Figure 2. PI is on the in-plane (x) axis, and PA is on the antiplane (y) axis. Shear stress, slip, and slip velocity are shown for solutions DFM0.05, DFM0.1, and BI0.1. The time histories of BI0.1 and DFM0.05 are virtually identical, with DFM0.1 also very close.

(antiplane direction) (Figure 9) confirm that the three solutions are virtually identical in their simulation of each of the principal processes of the rupture: initiation, evolution and stopping of the slip, and the evolution of the stress after the slipping ceases. All three solutions are plotted at the same scale in Figures 8 and 9. As shown in Figures 8 and 9, the pulses associated with the P and S waves returning from the borders of the fault are observed in the time histories of slip rate and stress. In Figures 8 and 9 we annotate these fault-edge-generated pulses. The P waves from the left and right borders of the fault traveling along the in-plane direction are denoted by "P" in Figure 8. The pulses associated with the edge-generated S wave are indicated by "Si" and "Sa," with Si corresponding to the pulses coming back from the left and right borders of the fault, traveling predominantly along the in-plane direction, and Sa corresponding to the pulses coming back from the top and bottom borders, traveling predominantly along the antiplane direction. In addition to these stopping phases, a late reactivation of slip, after its initial arrest, can also be seen in Figures 8 and 9 (and Figure 7 as noted previously). This feature is associated with the Si pulse, and its behavior is explained as follows. The P wave coming back from the boundary reduces the shear stress on the fault, causing slip to stop, leaving the shear stress somewhat below the dynamic friction value (dynamic overshoot). The subsequent Si fault edge pulse has to overcome that stress deficit in order to reinitiate slip. As it approaches the center of the fault, this pulse becomes weak. This wave experiences constructive interference at the center of the fault in which there is an encounter between the Si waves coming from the left and right side of the fault. As can be seen in the figures of shear stress, the Si pulse crosses the center and continues traveling to the other side of the fault, but always below the dynamic friction level, and therefore unable to produce further slipping. Note that our solution procedure assumes, for simplicity, that once the dynamic frictional strength τ_d is reached at a point on the fault, the strength will not increase to larger values on the timescale of the computation, even if the point reaches zero slip velocity. That is, it is assumed that there is no healing for times of order seconds. However, rock interfaces in the lab do exhibit healing at rest or small

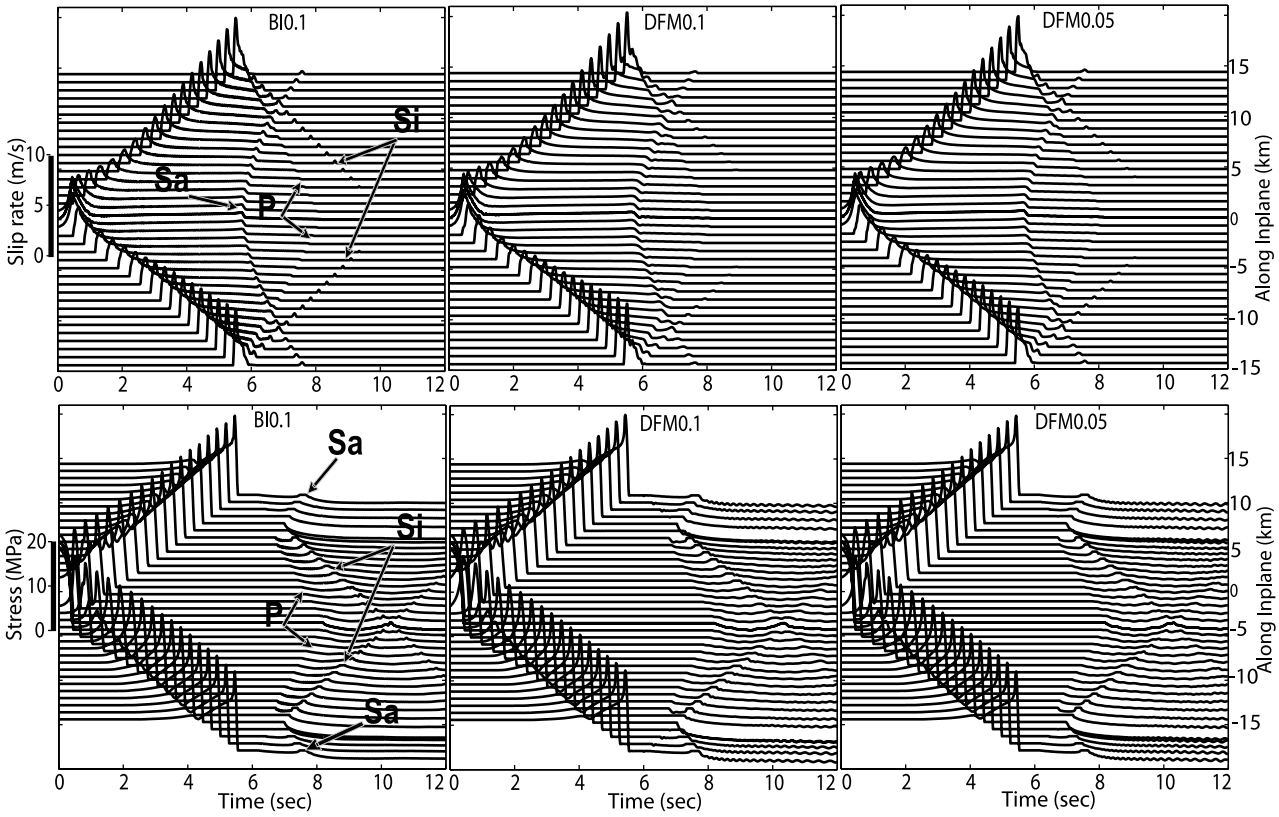

Figure 8. Time history of (top) slip rate and (bottom) shear stress for points along the axis of in-plane motion (x axis). The (left) BI0.1, (middle) DFM0.1, and (right) DFM0.05 solutions are shown. The labels P and Si correspond to the P and S waves, respectively, generated at the left and right edges of the fault (i.e., propagating predominantly along the axis of in-plane motion). The label Sa identifies the S waves generated at the top and bottom of the fault (propagating predominantly along the antiplane axis).

sliding velocities, and a more complete constitutive description would include that effect.

[59] To summarize, high-resolution DFM and BI solutions to the test problem are very close quantitatively, and the resulting features of spontaneous rupture propagation and arrest make sense qualitatively. BI0.1 and DFM0.05 agree in virtually every detail of timing and amplitude. DFM0.1 performs nearly as well. Results for DFM0.1 and DFM0.05, taken together, are consistent with the criterion $N_c \geq \sim 5$ for obtaining, in DFM solutions, slip rates free of artifacts and grid size independent to within a few percent, provided the criterion is satisfied uniformly over the fault. For BI solutions, the corresponding criterion is $N_c \geq \sim 3$.

8. Discussion

[60] We interpret the agreement between the highest-resolution BI and DFM solutions presented above as important evidence that both solutions are accurate approximations to the continuum solution of the spontaneous rupture problem that we posed. This interpretation is further supported by the level of grid interval independence achieved in the DFM and BI solutions.

8.1. Resolution Criterion

[61] On the basis of the size of the cohesive zone observed in these solutions, we propose that $N_c \approx 5$ or about five cells within the cohesive zone is sufficient to ensure an accurate (in the sense of the tolerances implied by Table 3) solution by the DFM method. The BI method is capable of similar accuracy with only about three cells within the cohesive zone ($N_c \approx 3$). Note that N_c represents a local, varying quantity, and the cohesive zone resolution by about five cells for DFM and three cells for BI should be achieved everywhere locally, i.e., that should be the resolution of the minimum cohesive zone size encountered.

[62] The criterion for uniform adherence to $N_c \geq 5$ for DFM and $N_c \geq 3$ for BI can probably be relaxed somewhat in many practical applications. The DFM0.1 velocity fluctuations have no effect on rupture propagation or arrest; and they decay quickly, so they do not represent an instability. Therefore they do not interact nonlinearly with the solution. For most purposes, therefore it would be adequate to remove them by low-pass filtering to attenuate Fourier components with wavelength shorter than the cohesive zone width. The same applies to BI0.15 (the time histories for which are not included in Figure 7 for clarity of plots). In that band-limited sense, DFM0.1 or BI0.15, although they do not quite satisfy the above criterion everywhere (since $N_c^{\min} = 3.3$ for DFM0.1 and $N_c^{\min} = 2.2$ for BI0.15), still provide accurate and artifact-free solutions. On the other hand, velocity fluctuations at the level present in DFM0.1 or BI0.15 might not be acceptable when using friction models with a sensitive dependence of stress on slip velocity. In the

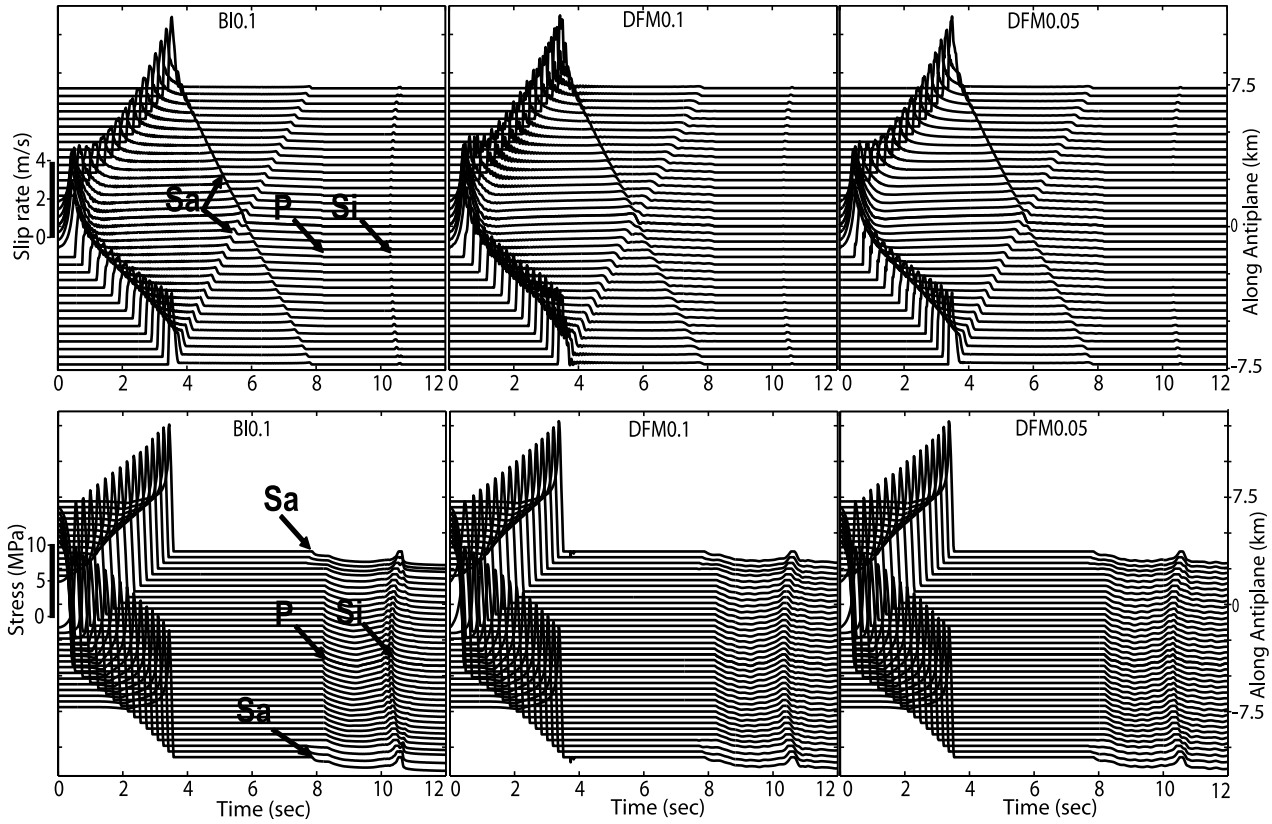

Figure 9. Time history of (top) slip rate and (bottom) shear stress for points along the axis of antiplane motion (y axis). The (left) BI0.1, (middle) DFM0.1, and (right) DFM0.05 solutions are shown. The labels P, Si, and Sa have the same meanings as in Figure 8.

case of rate- and state-dependent friction models [e.g., *Dieterich*, 1979; *Ruina*, 1983], for example, it might prove necessary to adhere strictly to our proposed resolution criterion.

[63] While it is reasonable to apply the obtained criterion for N_c to the class of problems considered here, in which the cohesive zone width is the smallest physical length scale present, the results will not extend to spontaneous rupture problems in which other, smaller characteristic length scales emerge. An example of the latter is the problem of rupture at a bimaterial interface. In that example, the coupling of shear and normal stress changes on the fault plane, combined with memory effects in the dependence of friction on normal stress, introduces an additional length scale [*Cochard and Rice*, 2000; *Ranjith and Rice*, 2001]. We conjecture that in such cases, our criterion of $N_c \sim 5$ for DFM and $N_c \sim 3$ for BI would still apply, provided, however, that N_c is redefined in terms of the new minimum physical scale of the problem.

8.2. Scale Collapse

[64] The cohesive zone shrinks upon the approach of rupture speed to a terminal value (the shear wave speed in the antiplane direction, the Rayleigh wave speed in the in-plane direction) as follows from (30). The cohesive zone contraction could potentially make it difficult to maintain N_c sufficiently large to ensure accuracy. In the antiplane direction, the simplest case, the cohesive zone width will collapse as $(1 - v^2/\beta^2)^{1/2}$, where v is the rupture velocity. In our test problem, v reaches $\sim 0.7\beta$ along the antiplane axis direction. The Lorentz factor would be reduced by an additional factor of about 2, for example, if rupture accelerated to $\sim 0.93\beta$ and by about a factor of 4 for $v \sim 0.98\beta$, reducing N_c in each simulation by these same factors. Thus dealing with rupture very near terminal speed is likely to be a significant challenge for rupture simulation.

[65] The approximate analysis (26)–(37) of the Lorentz contraction (in the context of the simple slip-weakening parameterization of friction) shows, for the antiplane direction, that the cohesive zone width scales with $(\mu d_0/\Delta\tau)^2 L^{-1}$ and, for a given $\Delta\tau$, it is nearly independent of the relative strength parameter S, as long as the propagation distance L is large compared with the critical dimension for crack instability. This is identical to the scaling that *Andrews* [1976, 2004] derived from a somewhat different (but essentially equivalent) line of reasoning. The stress drop $\Delta\tau$ used in our test calculation, 7 MPa, is about twice the average stress drop for shallow crustal earthquakes, making the test case modestly conservative in this respect (that is, had we used a more typical stress drop value of 3 MPa, the cohesive zone sizes and hence N_c would have been larger). The influence of the propagation-distance factor L on the cohesive zone size is limited by the fault width and the scale of the largest asperities. Our cohesive zone consideration (26)–(39) is restricted to 2-D cases but, in 3-D, the smaller dimension (width) of the fault will ultimately put a bound on the stress intensity factor through which L enters the cohesive zone analysis. Our test problem has a fault width of 15 km, which is representative of the fault width for

shallow crustal earthquakes. This fault width value is equal to the maximum along-strike propagation distance of 15 km in the test problem, and the influence of the propagation distance factor is therefore probably already at or near its limiting value [*Day*, 1982a]. That is, even a much longer fault would not lead to much further scale contraction, so the test problem is probably also conservative with respect to the propagation distance factor. The characteristic displacement d_0, however, is very uncertain, and values much lower than our test problem value of 0.4 m are plausible. A d_0 value of 0.1 m, for example, would have reduced N_c in each of our test problem simulations by a factor 16, putting our DFM criterion of $N_c \sim 5$ and BI criterion of $N_c \sim 3$ practically out of reach for a numerically tractable calculation.

[66] Other factors, however, may limit the scale collapse associated with the approach to terminal velocity, and thus work in favor of numerical resolution (i.e., increased N_c). Contraction of the cohesive zone is accompanied by very high strains near the fault. In an elastic model, stresses near the fault will grow inversely with the cohesive zone dimension [*Rice*, 1980], and in a more realistic model, at some stage of the cohesive zone collapse, additional energy losses will occur in the form of inelastic work off the fault surface. These losses, if modeled, would limit the collapse of the cohesive zone. In the DFM simulations, the artificial viscosity provides a dissipation mechanism that takes the place of such unmodeled energy losses and thereby limits the collapse of the cohesive zone length scale [*Day and Ely*, 2002]. This procedure is analogous to the viscous regularization of shock waves calculations [e.g., *Gustafsson et al.*, 1995]. *Andrews* [2004] demonstrates some alternative methods that limit scale collapse, in the context of perfect elasticity, by modifications to the friction law. Rupture simulations that incorporate off-fault inelastic losses [*Dalgueret al.*, 2003a, 2003b; *Andrews*, 2005] provide theoretical justification for these procedures. In the simulations of Dalguer et al., for example, off-fault tension cracks open during shear rupture. This off-fault dissipation mechanism results in a reduction of the rupture velocity. Similarly, Andrews' inelastic simulations show that when realistic off-fault inelastic energy losses are considered, fracture energy is not a constant, but rather increases with propagation distance (as does an equivalent slip-weakening displacement derived from an auxiliary elastic calculation), mitigating the collapse of scale lengths at the rupture front. When nonlinear material behavior off the fault plane dominates the energy dissipation, an appropriate length scale from which to define N_c will likely be the characteristic length over which the inelastic dissipation rate is appreciable.

8.3. Computational Resources Required and Associated Parameter Limitations

[67] The 3-D spontaneous rupture calculations are quite challenging in terms of required memory and processor power. Let us consider only the memory (RAM) requirements here, as this is often the limiting factor. The memory required is 17.5 GB for BI0.1, 2.3 GB for DFM0.1, and 17.8 GB for DFM0.05. Note that the memory requirement for BI0.1 can be significantly reduced, to 2–3 GB, by using justifiable truncation of the dynamic response (e.g., as discussed by *Lapusta et al.* [2000] for a 2-D case), which was not used here to assure the most accurate BI solution. The amount of memory needed scales with the inverse cube of the grid spacing Δx for both methods. Note that high-resolution runs for both methods were done on multiple processors using message passing (MPI).

[68] Hence we immediately see the challenge in terms of computer resources one faces in studies of spontaneous ruptures. For example, suppose we would like to keep the same fracture energy in our problem, but study the effect of considering ξ times smaller critical slip d_0 (and changing the frictional properties accordingly). Then, for the same stress drop, the cohesive zone sizes we would need to resolve would decrease ξ^2 times according to (37). This means that we would need to decrease Δx by a factor of ξ^2, for a total increase in memory by a factor of ξ^6. That means that just halving d_0 would require 64 times as much memory, or about 150 GB for DFM and BI with truncation, and 1.1 TB for BI without truncation, which is already the scale of the largest supercomputers. Taking 10 times smaller d_0 would require 1,000,000 times more memory and would clearly be impossible with present-day computers.

8.4. Significance of DFM/BI Agreement

[69] Establishing the accuracy of numerical solution methods for the spontaneous rupture problem is challenging principally because of the nonlinearity of the problem. That nonlinearity is attributable mainly to the fact that rupture evolution and arrest are not specified a priori. In other words, we have a mixed boundary value problem in which the respective (time-dependent) domains of displacement and traction boundary conditions are themselves dependent upon the displacement and stress fields. Nonlinearity allows phenomena to arise that are absent in idealized tests on linear problems but pose significant challenges for a numerical method; the problem of scale contraction discussed above being an important example.

[70] No analytical solutions are known for 3-D spontaneous rupture problems, apart from a few special cases that reduce to linear problems (e.g., the nucleation phase solution of *Campillo and Ionescu* [1997]) and are thus inappropriate for our purpose. We are therefore forced to make inferences about accuracy from comparison of numerical solutions. The BI method, however, could be legitimately viewed as providing at least a semianalytical characterization of the solution to the limited class of problems to which it is applicable. The BI solution does represent the fault plane traction and velocity discontinuity discretely, and requires purely numerical manipulations to satisfy the jump conditions. However, it represents the continuum response to a given velocity discontinuity exactly, by means of a closed form Green's function. It is therefore not subject to the main form of error present in volume discretization methods such as the DFM method, which is numerical dispersion. For this reason, we would argue that agreement between DFM and BI solutions is stronger evidence of numerical accuracy (of both methods) than would be agreement between two different volume discretization codes alone.

[71] The convergence rates of the two methods are nearly indistinguishable, as indicated by their approximately equal slopes in Figures 4 and 5. It is perhaps surprising that a low-order finite difference method such as DFM performs as

well as it does relative to the semianalytical BI method on this problem. We do not have a complete explanation for this result but make several observations:

[72] 1. The spontaneous rupture solution is discontinuous in the displacement and velocity fields. Therefore nominally higher-order finite difference methods will not actually achieve higher-order accuracy for this problem unless they incorporate separate, one-sided high-order difference templates on each side of the fault plane (this can be done quite naturally with high-order finite elements or spectral elements, but has not been attempted in higher-order finite difference solutions). Thus a second-order finite difference scheme like DFM is not at any obvious disadvantage relative to high-order finite difference methods.

[73] 2. The specific method used to treat the jump condition appears to be more important than the differencing scheme used at interior nodes. We have found [*Dalguer and Day*, 2004] that the traction-at-split-node (TSN) method used in DFM converges substantially better than the alternative stress glut (SG) [*Andrews*, 1999] and thick fault (TF) [*Madariaga et al.*, 1998] methods. To achieve results comparable to those from the TSN method with $\Delta x = h$, for example, the SG method requires a $\Delta x = h/2$, and the TF method requires $\Delta x < h/4$. Stated differently, the required resolution ratio N_c is roughly twice as large for method SG, and at least 4 times as large for method TF, as it is for the TSN method tested in this paper.

[74] 3. The DFM implementation of the TSN method incorporates an added artificial viscosity [*Day and Ely*, 2002] of Kelvin-Voigt form, characterized by a parameter $\overline{\eta}$ (Appendix A, equation (A8)). The damping is artificial in the sense that it is part of the numerical procedure for solving the perfectly elastic problem, and is not intended to represent a physical damping. This damping term selectively suppresses short-wavelength oscillations arising from the use of a low-order difference approximation. The damping parameter is dimensionless, and, for fixed $\overline{\eta}$. the absorption-wavelength spectrum scales in proportion to the grid interval Δx. A damping parameter $\overline{\eta}$ equal to 0.1 was used with DFM in these tests. Values substantially higher than this value visibly degrade the sharpness with which shear stress is resolved at the rupture front in the $\Delta x = 0.1$ km case, with adverse effects on rupture timing. For example, using an $\overline{\eta}$ value of 0.3 instead of the preferred value of 0.1 results in a slight (less than 1.5%) reduction of the average rupture velocity in the DFM0.1 test. The effect of using a higher damping value is negligible in the higher-resolution DFM0.05 test, however, reflecting the fact that the absorption band shifts to shorter (by a factor of 2) wavelengths in that case, and these components are already significantly attenuated by the cohesive zone. At the other extreme, using zero damping results in a DFM0.1 solution so oscillatory that early arrest and rerupture can occur spuriously at some fault points.

[75] The BI/DFM comparisons presented here complement experimental tests of the DFM finite difference solutions by *Day and Ely* [2002]. In those tests, numerical simulations reproduced the shape, timing, and duration of acceleration pulses recorded adjacent to the fault surface in the scale model earthquake experiments of *Brune and Anooshehpoor* [1998]. In combination, these very different types of tests provide strong evidence of convergence of both the BI and DFM solutions to the continuum solution. Of course, in both cases the emphasis has been on validation of the numerical methods themselves; neither type of test addresses the relevance of the underlying theoretical formulation to the rupture process of natural earthquakes.

[76] We note that both methods examined here are rather limited in the class of problems that they can address. The BI method, at least in the implementation presented here, is limited to uniform infinite space problems, and the DFM method, although it can address problems with a free surface and complex material properties, is limited with respect to admissible fault geometry (i.e., piecewise planar segments, all parallel to a single coordinate plane). The numerical results presented here have been shown to be independent of both grid size and solution method, to within well-quantified tolerances, and may therefore provide a useful starting point for testing newer, more capable numerical methods for spontaneous rupture.

9. Conclusions

[77] A traction-at-split-node finite difference method (DFM) and a boundary integral method (BI) give virtually indistinguishable solutions to a spontaneous rupture test problem (SCEC benchmark problem, version 3 [*Harris et al.*, 2004]) when both methods adequately resolve the cohesive zone (i.e., with at least five node points for DFM and at least three cells for BI). Qualitatively, both solutions are virtually identical in their simulation of initiation, evolution and stopping of the slip, and the evolution of the stress after the slipping ceases. Quantitatively, we have assessed agreement between the methods in terms of the RMS differences in rupture time, final slip, and peak slip rate, and related these to median ($\overline{N}_c$) and minimum ($N_c^{\min}$) resolution measures. With $\overline{N}_c = 4.4$ (and $N_c^{\min} = 3.3$) for both methods, the RMS time, slip, and slip rate differences are 0.8%, 0.6%, and 9%, respectively. With the same $\overline{N}_c$ and $N_c^{\min}$ for BI, but better resolution ($\overline{N}_c = 8.7$ and $N_c^{\min} = 6.5$) for DFM, these metrics are 0.8%, 0.4%, and 3%, respectively.

[78] Furthermore, calculations over approximately an order of magnitude range in $\overline{N}_c$ demonstrate a well-defined power law asymptotic behavior of both the DFM and BI solutions: for each method, variations of predicted rupture time with respect to grid spacing follow a power law with exponent $\sim$3. We interpret this behavior, combined with the agreement between BI and DFM solutions, as evidence of asymptotic convergence to the continuum solution. The final slip and peak slip rate metrics show similar power law behavior, with exponents between 1 and 2 for both methods.

[79] The ability of a low-order DFM finite difference method to match the boundary integral solution with only about five nodes resolving the cohesive zone calls into question the advantages of high-order differencing schemes for this problem. In fact, nominally high-order methods will actually have truncation errors of the same order as nominally lower-order methods for this problem, since the displacement field is itself discontinuous. Artificial viscosity adequately controls the numerical oscillations that are inherent in the low-order difference scheme. The DFM solution with $\overline{N}_c = 4.4$ has a weak but measurable sensitiv-

ity to large departures of the damping parameter $\overline{\eta}$ from our preferred value of 0.1 (i.e., tripling $\overline{\eta}$ slows rupture by an amount everywhere less than 1.5%). The sensitivity to $\overline{\eta}$ diminishes with increasing resolution length N_c, reflecting the fact that the artificial damping is scale selective, with the scale set by the grid interval.

[80] These numerical tests help fill a gap in our understanding of the accuracy of numerical solutions to nonlinear spontaneous rupture problems. In addition, the solutions presented here, by virtue of being demonstrably grid-independent and consistent between two very different numerical methods, may prove useful for testing new numerical methods for spontaneous rupture.

Appendix A: Finite Difference Equations

[81] The grid is defined by a set of index triples $Q = [i_x, i_y, i_z]$ where i_x, i_y, and i_z are integers. The grid node point corresponding to Q is at $\mathbf{r}_Q$, which is given in terms of Cartesian unit vectors $\hat{\mathbf{e}}_\nu$, $\nu = x, y, z$, and three orthogonal sets of coordinate planes defined by indexed sets of coordinates, $(r_\nu)_{i_\nu}$, $i_\nu = 1, \ldots, L_\nu$. $\nu = x, y, z$:

$$\mathbf{r}_Q = \sum_\nu (r_\nu)_{i_\nu} \hat{\mathbf{e}}_\nu. \tag{A1}$$

Displacement and velocity vectors at the node points are similarly denoted

$$\mathbf{u}_Q \equiv \sum_\nu u_\nu(\mathbf{r}_Q)\hat{\mathbf{e}}_\nu \tag{A2}$$

and

$$\dot{\mathbf{u}}_Q \equiv \sum_\nu \dot{u}_\nu(\mathbf{r}_Q)\hat{\mathbf{e}}_\nu. \tag{A3}$$

Cell centers are denoted by indices $\tilde{Q} = [i_x + 1/2, i_y + 1/2, i_z + 1/2]$. The cell dimensions Δr_ν and cell volume V carry index $\tilde{Q}$, and are defined by

$$(\Delta r_\nu)_{\tilde{Q}} \equiv (r_\nu)_{i_\nu+1} - (r_\nu)_{i_\nu} \tag{A4}$$

and

$$V_{\tilde{Q}} \equiv \prod_\nu (\Delta r_\nu)_{\tilde{Q}}. \tag{A5}$$

Material properties ρ, α, and β (density, P and S wave speeds, respectively) are likewise indexed to the cell centers, as are the numerical viscosities and hourglass suppression constants $\overline{\eta}$, $\overline{\chi}$, and $\overline{Y}$ introduced below (so that constants that serve to regularize the numerical scheme, rather than to represent physical properties, are distinguished by overbars).

[82] We define the index increment D by $D \equiv [d_x/2, d_y/2, d_z/2]$, where each d_ν can be either 1 or -1, so that D has eight possible values. We define index addition in the obvious way, such that for example, $Q + D = [i_x + d_x/2, i_y + d_y/2, i_z + d_z/2]$, and introduce the convention that in any equation containing D on the right-hand side (but not the left-hand side), there is an implied summation of the right-hand side over all eight possible D values.

[83] The discrete strain and stress tensors, $\boldsymbol{\varepsilon}$ and $\boldsymbol{\sigma}$, carry cell index $\tilde{Q}$, and are given by, respectively,

$$\boldsymbol{\varepsilon}_{\tilde{Q}} = \frac{1}{2}\sum_\nu \frac{d_\nu}{4(\Delta r_\nu)_{\tilde{Q}}}\left(\hat{\mathbf{e}}_\nu \mathbf{u}_{\tilde{Q}+D} + \mathbf{u}_{\tilde{Q}+D}\hat{\mathbf{e}}_\nu\right) \tag{A6}$$

and

$$\boldsymbol{\sigma}_{\tilde{Q}} = \rho_{\tilde{Q}}\left(\alpha_{\tilde{Q}}^2 - 2\beta_{\tilde{Q}}^2\right)\mathbf{tr}\left(\boldsymbol{\varepsilon}_{\tilde{Q}}\right)\mathbf{I} + 2\rho_{\tilde{Q}}\beta_{\tilde{Q}}^2\boldsymbol{\varepsilon}_{\tilde{Q}}. \tag{A7}$$

An artificial viscosity is also introduced, leading to damping stress tensor $\overline{\boldsymbol{\sigma}}$,

$$\overline{\boldsymbol{\sigma}}_{\tilde{Q}} = \overline{\eta}_{\tilde{Q}}\Delta t\left[\rho_{\tilde{Q}}\left(\alpha_{\tilde{Q}}^2 - 2\beta_{\tilde{Q}}^2\right)\mathbf{tr}\left(\dot{\boldsymbol{\varepsilon}}_{\tilde{Q}}\right)\mathbf{I} + 2\rho_{\tilde{Q}}\beta_{\tilde{Q}}^2\dot{\boldsymbol{\varepsilon}}_{\tilde{Q}}\right], \tag{A8}$$

where $\overline{\eta}$ is a cell-indexed dimensionless damping constant. Null, or hourglass, modes [e.g., *Hughes*, 1987, p. 239] are stabilized by addition of stiffness and damping forces that oppose the motion of the null modes. Cell-indexed hourglass mode amplitudes $\mathbf{H}^i$, i = 1, ..., 4, are given by

$$\mathbf{H}_{\tilde{Q}}^i = \sum_\nu \hat{\mathbf{e}}_\nu A_D^i \frac{\hat{\mathbf{e}}_\nu}{(\Delta r_\nu)_{\tilde{Q}}^2} \cdot \left(\mathbf{u}_{\tilde{Q}+D} + \bar{\chi}_{\tilde{Q}}\Delta t\dot{\mathbf{u}}_{\tilde{Q}+D}\right), \tag{A9}$$

where

$$A_D^1 = d_x d_y d_z, \quad A_D^2 = d_x d_y, \quad A_D^3 = d_y d_z, \quad A_D^4 = d_x d_z. \tag{A10}$$

The cell hourglass amplitudes are volume-weighted to compute the null mode resistance force $\mathbf{F}$ at the nodes,

$$\mathbf{F}_Q = -\bar{Y}_{Q+D}V_{Q+D}\sum_i A_D^i \mathbf{H}_{Q+D}^i. \tag{A11}$$

The constants $\overline{\chi}$ (dimensionless) and $\overline{Y}$ (same dimensions as stress) are hourglass damping and stiffness constants, respectively. We set $\overline{\chi} = 0.7$, and $\overline{Y} = \frac{1}{12}\rho\beta^2(1 - \beta^2/\alpha^2)$, the latter motivated by the finite element treatment of *Kosloff and Frazier* [1978]; results are not very sensitive to the precise values, so long as they are large enough to suppress growth of the null modes.

[84] A nodal mass M and restoring force vector $\mathbf{R}$ are indexed to the node points,

$$M_Q \equiv \frac{1}{8}V_{Q+D}\rho_{Q+D} \tag{A12}$$

and

$$\mathbf{R}_Q \equiv V_{Q+D}\sum_\nu \frac{d_\nu}{4(\Delta r_\nu)_{Q+D}}\hat{\mathbf{e}}_\nu \cdot \left(\boldsymbol{\sigma}_{Q+D} + \bar{\boldsymbol{\sigma}}_{Q+D}\right) + \mathbf{F}_Q. \tag{A13}$$

Equating restoring forces and inertial forces, approximating by central differences with time step Δt, and integrating leads to

$$\dot{\mathbf{u}}_Q(t + \Delta t/2) = \dot{\mathbf{u}}_Q(t - \Delta t/2) + \Delta t M_Q^{-1}\mathbf{R}_Q(t) \tag{A14}$$

and

$$\mathbf{u}_Q(t+\Delta t) = \mathbf{u}_Q(t) + \Delta t \dot{\mathbf{u}}_Q(t+\Delta t/2). \tag{A15}$$

We use $\mathbf{u}(t)$ and $\dot{\mathbf{u}}(t-\Delta t/2)$ to compute all terms in $\mathbf{R}(t)$, so the scheme is fully explicit.

[85] At a fault plane, we split each node-centered quantity (i.e., those indexed by Q) into plus- and minus-side parts, $\mathbf{u}^{\pm}$, $\dot{\mathbf{u}}^{\pm}$, $\mathbf{F}^{\pm}$, $M^{\pm}$, and $\mathbf{R}^{\pm}$. The latter three pairs of quantities are defined by splitting the summations on D in each of (A11), (A12), and (A13) into two parts. This partitioning is done by introducing $D^{\pm} \equiv [{}^{d_x}\!/_2, {}^{d_y}\!/_2, {}^{\pm 1}\!/_2]$, where d_x and d_y can be either 1 or -1, so that each index set (i.e., D^+ or D^-) has four possible values. With the convention that summation over the four possible values of D^+ or D^- is implied in any equation that contains either D^+ or D^-, with d_z fixed at $d_z = +1$ for D^+ summations and fixed at $d_z = -1$ for D^- summations, we define the following split node quantities:

$$\mathbf{F}^{\pm}_Q \equiv -\bar{Y}_{Q+D^{\pm}} V_{Q+D^{\pm}} \sum_i A^i_{D^{\pm}} \mathbf{H}^i_{Q+D^{\pm}}, \tag{A16}$$

$$M^{\pm}_Q \equiv \frac{1}{8} V_{Q+D^{\pm}} \rho_{Q+D^{\pm}}, \tag{A17}$$

$$\mathbf{R}^{\pm}_Q \equiv V_{Q+D^{\pm}} \sum_\nu \frac{d_\nu}{4(\Delta r_\nu)_{Q+D^{\pm}}} \hat{\mathbf{e}}_\nu \cdot \left(\boldsymbol{\sigma}_{Q+D^{\pm}} + \bar{\boldsymbol{\sigma}}_{Q+D^{\pm}}\right) + \mathbf{F}^{\pm}_Q. \tag{A18}$$

We then introduce the traction vector $\mathbf{T}$ acting at fault plane nodes, and nodal area a defined by

$$a_Q = (4\Delta r_z)^{-1}_{Q+D^+} V_{Q+D^+}. \tag{A19}$$

We denote the initial equilibrium value of $\mathbf{T}$ by $\mathbf{T^0}$. Equating restoring forces and inertial forces separately for the two sides of the split nodes gives the split node counterparts of (A14) and (A15),

$$\dot{\mathbf{u}}^{\pm}_Q(t+\Delta t/2) = \dot{\mathbf{u}}^{\pm}_Q(t-\Delta t/2) + \Delta t \left(M^{\pm}_Q\right)^{-1} \cdot \left\{\mathbf{R}^{\pm}_Q(t) \mp a_Q\left[\mathbf{T}_Q(t) - \mathbf{T}^0_Q\right]\right\} \tag{A20}$$

and

$$\mathbf{u}^{\pm}_Q(t+\Delta t) = \mathbf{u}^{\pm}_Q(t) + \Delta t \dot{\mathbf{u}}^{\pm}_Q(t+\Delta t/2). \tag{A21}$$

The traction vector $\mathbf{T}$ is determined from the jump conditions and the friction model, as described in the main text.

Appendix B: Equations of Boundary Integral Method

B1. Space and Time Discretization

[86] We would like to compute the evolution of slip (or tangential displacement discontinuities) and stresses on a rectangular domain of a planar interface embedded in an infinite homogeneous isotropic elastic solid. In particular, the slip accumulation may take the form of a shear crack or rupture propagating along the interface. We introduce the Cartesian coordinate system (x, y, z) such that the interface corresponds to $z = 0$ and x and y are directed along the axis of symmetry of the rectangular domain under consideration. The domain has dimensions λ_x and λ_y in the x direction and y direction, respectively.

[87] We discretize the domain into $L_x \times L_y$ cells, where L_x and L_y are even, as required by (19). In general, the cells can be rectangular, but here we choose the number of cells so that they are square, and hence

$$\lambda_x/L_x = \lambda_y/L_y = \Delta x.$$

The size of the cells Δx determines the spatial discretization. The field variables such as stress, slip, slip rate, etc. are considered to be constant throughout the cell.

[88] The time step Δt is constant and is taken as a fraction of time needed for the shear wave to propagate through one cell in x or y direction, in the form

$$\Delta t = \gamma \Delta x/\beta.$$

Usually we take $\gamma = 1/4$ to $1/2$. $\gamma = 1/3$ is used for the simulations presented here. Note that it is possible to use variable time step in this formulation and this has been done in studies of earthquake sequences where both slow deformation periods between earthquakes and fast dynamic ruptures during earthquakes are involved [*Ben-Zion and Rice*, 1997; *Lapusta et al.*, 2000].

[89] Since the spectral formulation (18)–(23) used here replicates (or periodically repeats) the domain of interest, the domain dimensions λ_x and λ_y should be sufficiently larger than the area over which active slipping takes place to prevent replications affecting each other through elastic waves. In the test case considered in this work, the rupture spreads over the area 30 km × 15 km. The presented results were obtained using $\lambda_x = 60$ km and $\lambda_y = 45$ km. Using larger values for the run with $\Delta x = 0.3$ km did not affect the results.

B2. Computational Cycle

[90] To update field variables over one time step Δt, we use the scheme developed and presented by *Lapusta et al.* [2000], with suitable modifications. The work of *Lapusta et al.* [2000] involved a two-dimensional antiplane problem, rate and state friction laws, and variable time step. Here we consider a 3-D problem with slip-weakening friction and constant time step. We briefly describe the modified updating scheme in the following.

[91] Suppose that at time t, the discretized values of tangential discontinuities (slips) $s_\nu(t; i, j)$, slip rates (or velocities) $\dot{s}_\nu(t; i, j)$, $\nu = x, y$, and slip path length $\ell(t; i, j)$ are known for all cells (i, j), $i = 1, 2, \ldots, L_x$, $j = 1, 2, \ldots, L_y$. In addition, the history of the slip rates is known in terms of their Fourier coefficients $\dot{S}_\nu(t'; k, m)$ for (discretized) prior time t', $0 < t' < t$, where $t = 0$ is the beginning of the deformation process considered, $k = -L_x/2, -L_x/2 + 1, \ldots, L_x/2$, $m = -L_y/2, -L_y/2 + 1, \ldots, L_y/2$. We also know the Fourier coefficients of slips S_ν $(t; k, m)$ which, as we will see, we should have obtained during the previous time step.

Then, to find the values of the field variables at time $t + \Delta t$, we proceed in the spirit of a second-order Runge-Kutta procedure as follows.

[92] 1. Make the first predictions of the values of the tangential discontinuities, s^*_ν $(t + \Delta t; i, j)$, their Fourier coefficients, S^*_ν $(t + \Delta t; k, m)$, slip path length, ℓ^* $(t + \Delta t; i, j)$, and stress transfer functionals, $f^*_\nu(t + \Delta t; i, j)$, at time $t + \Delta t$ assuming that the slip velocities stay constant and equal to $\dot{s}_\nu$ $(t; i, j)$ throughout the time step. Hence we start with

$$s^*_\nu(t+\Delta t;i,j) = s_\nu(t;i,j) + \Delta t \dot{s}_\nu(t;i,j),$$
$$S^*_\nu(t+\Delta t;k,m) = S_\nu(t;k,m) + \Delta t \dot{S}_\nu(t;k,m),$$
$$\ell^*(t+\Delta t;i,j) = \ell(t;i,j) + \Delta t\sqrt{\dot{s}^2_x(t;i,j) + \dot{s}^2_y(t;i,j)},$$

where S_ν $(t; k, m)$ are known and $\dot{S}_\nu$ $(t; k, m)$ are computed from $\dot{s}_\nu$ $(t; i, j)$ using fast Fourier transform (FFT). Then we compute the first predictions of the Fourier coefficients of the stress transfer functionals, $F^*{}_\nu$ $(t + \Delta t; k, m)$, using (23). Let us rewrite just one of the two analogous terms on the right-hand side of (19). We get

$$\begin{Bmatrix} F^*_x(t+\Delta t;k,m) \\ F^*_y(t+\Delta t;k,m) \end{Bmatrix}$$
$$= -\frac{\mu}{2q}\begin{bmatrix} \hat{k}^2 & \hat{m}\hat{k} \\ \hat{m}\hat{k} & \hat{m}^2 \end{bmatrix}\left(2\left(1-\frac{\beta^2}{\alpha^2}\right)\begin{Bmatrix} S^*_x(t+\Delta t;k,m) \\ S^*_y(t+\Delta t;k,m) \end{Bmatrix}\right)$$
$$-\frac{\mu}{2q}\begin{bmatrix} \hat{k}^2 & \hat{m}\hat{k} \\ \hat{m}\hat{k} & \hat{m}^2 \end{bmatrix}\left(-\int_{\Delta t}^{t+\Delta t} K_{II}(q\beta t')\begin{Bmatrix} \dot{S}_x(t+\Delta t-t';k,m) \\ \dot{S}_y(t+\Delta t-t';k,m) \end{Bmatrix}\mathrm{d}t'\right)$$
$$-\frac{\mu}{2q}\begin{bmatrix} \hat{k}^2 & \hat{m}\hat{k} \\ \hat{m}\hat{k} & \hat{m}^2 \end{bmatrix}\left(-\begin{Bmatrix} \dot{S}_x(t;k,m) \\ \dot{S}_y(t;k,m) \end{Bmatrix}\int_0^{\Delta t} K_{II}(q\beta t')\mathrm{d}t'\right)$$
$$+ \text{ similarly rewritten second term of (23).}$$

The second line at the right-hand side of the above expression can be computed, since the slip velocity history in terms of Fourier coefficients is known. The third line gives an approximation of the convolution on the time interval corresponding to the current step. We use the extended midpoint integration scheme [e.g., *Press et al.*, 1986] to compute the convolution integrals. The convolution integrals involve kernels given by (22)–(23). We precalculate (and store) the kernels using the expressions from (22)–(23) with finite integrals, the extended trapezoidal rule to evaluate the integrals, and subroutines from Numerical Recipes [*Press et al.*, 1986] to evaluate Bessel functions. Finally, we compute the first predictions of stress transfer functionals, f^*_ν $(t + \Delta t; i, j)$, using their Fourier coefficients F^*_ν $(t + \Delta t; k, m)$ and an inverse FFT.

[93] 2. Find the first prediction of slip rates, $\dot{s}^*_\nu$ $(t + \Delta t; i, j)$, corresponding to the predicted slip ℓ^* $(t + \Delta t; i, j)$ and functionals f^*_ν $(t + \Delta t; i, j)$, by making the tractions (18) agree with the frictional strength and jump conditions. To accomplish that, we consider two cases, depending on whether the slip rates are zero or nonzero during the current time step (i.e., the time step that spans the time interval $(t, t + \Delta t)$. Let us denote by τ^0_c $(t + \Delta t; i, j)$ the frictional strength which the cell (i, j) would have at time $t + \Delta t$ if its slip rates were zero during the current time step. We can compute τ^0_c $(t + \Delta t; i, j)$ from (5)–(6) as

$$\tau^0_c(t+\Delta t;i,j) = \begin{cases} -\sigma_n[\mu_s - W\ell(t;i,j)] & \text{if } \ell(t;i,j) \le d_0 \\ -\sigma_n\mu_d & \text{if } \ell(t;i,j) > d_0 \end{cases},$$

where $W = (\mu_s - \mu_d)/d_0$ is the slope of the slip-weakening part of the friction law (6).

[94] In case 1, for the slip rates to be zero at time $t + \Delta t$, the zero rate frictional strength τ^0_c $(t + \Delta t; i, j)$ should be larger than the shear traction magnitude computed from (18) assuming zero slip rates, i.e., the following condition should hold:

$$\tau^0_c(t+\Delta t;i,j) > \sqrt{\Psi^{*2}_x(t+\Delta t;i,j) + \Psi^{*2}_y(t+\Delta t;i,j)}$$
$$\equiv \Psi^*(t+\Delta t;i,j),$$

where Ψ^*_ν $(t + \Delta t; i, j) = \tau^o_\nu$ $(t + \Delta t, i, j) + f^*_\nu(t + \Delta t, i, j)$ and τ^o_ν τ^o_ν $(t + \Delta t, i, j)$ are given. If the condition holds, we set $\dot{s}^*_\nu$ $(t + \Delta t; i, j) = 0$, $\nu = x, y$.

[95] In case 2, if τ^0_c $(t + \Delta t; i, j) \le \Psi^*$ $(\mathrm{t} + \Delta\ t; i, j)$, then the slip rates can be nonzero and we need to solve the following equations. The predicted frictional strength $\tau^*_c(t + \Delta t; i, j)$ should be equal to the magnitude of the shear traction vector:

$$\tau^*_c(t+\Delta t;i,j) = \sqrt{\tau^{*2}_x(t+\Delta t;i,j) + \tau^{*2}_y(t+\Delta t;i,j)}.$$

The frictional strength depends on the predicted value of the slip path length ℓ^* $(t + \Delta t; i, j)$ through the friction law (5)–(6):

$$\tau^*_c(t+\Delta t;i,j) = \begin{cases} -\sigma_n(\mu_s - W\ell^*(t+\Delta t;i,j)) \\ \quad \text{if } \ell(t+\Delta t;i,j) \le d_0 \\ -\sigma_n\mu_d \text{ if } \ell^*(t+\Delta t;i,j) > d_0 \end{cases}.$$

From (18), the predictions of the shear traction components are given by

$$\tau^*_\nu(t+\Delta t;i,j) = \Psi^*_\nu(t+\Delta t;i,j) - \frac{\mu}{2\beta}\dot{s}^*_\nu(t+\Delta t;i,j).$$

Finally, the sliding direction should coincide with the direction of the shear traction vector, or

$$\frac{\dot{s}^*_x(t+\Delta t;i,j)}{\dot{s}^*_y(t+\Delta t;i,j)} = \frac{\tau^*_x(t+\Delta t;i,j)}{\tau^*_y(t+\Delta t;i,j)}.$$

After algebraic manipulations, the above equations lead to the following expressions for the predicted rates $\dot{s}^*_\nu(t + \Delta t; i, j)$, $\nu = x, y$:

$$\dot{s}^*_\nu(t+\Delta t;i,j) = \Psi^*_\nu(t+\Delta t;i,j) \cdot \frac{1 - \tau^*_c(t+\Delta t;i,j)/\Psi^*(t+\Delta t;i,j)}{\mu/2\beta}.$$

If the cell (i, j) has slip path length less than d_0 at time t but larger than d_0 at time $t + \Delta t$, this calculation can result in slip rates $\dot{s}^*_\nu\ (t + \Delta t;\ i, j)$ that correspond to the (resolved) shear stress in the direction of motion lower than $\tau_d = -\sigma_n\ \mu_d$. This is because the above calculation for the time step Δt will be governed by the decreasing part of the friction law, and hence, at time $t + \Delta t$, this decreasing part may extend beyond slip d_0 and below the dynamic friction $\tau_d = -\sigma_n\ \mu_d$. Yet the resolved shear stress cannot be less than the frictional strength during sliding. To remedy that, we compute the resolved shear stress $\sqrt{\tau^{*2}_x(t + \Delta t; i,j) + \tau^{*2}_y(t + \Delta t; i,j)}$ that corresponds to the computed slip rates $\dot{s}^*_\nu\ (t + \Delta t;\ i, j)$ and, if the stress is less than $\tau_d = -\sigma_n\ \mu_d$, we reassign the stress to be equal to $\tau_d = -\sigma_n\ \mu_d$ and then recompute the corresponding $\dot{s}^*_\nu\ (t + \Delta t;\ i, j)$.

[96] 3. Make the second predictions of the values of tangential discontinuities, $s^{**}_\nu(t + \Delta t;\ i,\ j)$, their Fourier coefficients, $S^{**}_\nu\ (t + \Delta t;\ k,\ m)$, slip path length, $\ell^{**}\ (t + \Delta t;\ i, j)$, and stress transfer functionals, $f^{**}_\nu\ (t + \Delta t;\ i, j)$, at time $t + \Delta t$ assuming that the slip velocities stay constant and equal to $(\dot{s}_\nu\ (t;\ i, j) + \dot{s}^*_\nu\ (t + \Delta t;\ i, j))/2$ throughout the time step. Hence we iterate the second time on our solution, improving it. The steps are analogous to those in stage 1. For example, we now write

$$
\begin{aligned}
s^{**}_\nu(t + \Delta t; i,j) &= s_\nu(t; i,j) + \Delta t(\dot{s}_\nu(t; i,j) + \dot{s}^*_\nu(t + \Delta t; i,j))/2,\\
S^{**}_\nu(t + \Delta t; k,m) &= S_\nu(t; k,m) + \Delta t(\dot{S}_\nu(t; k,m)\\
&\quad + \dot{S}^*_\nu(t + \Delta t; k,m))/2,\\
\ell^{**}(t + \Delta t; i,j) &= \ell(t; i,j) + \Delta t\\
&\cdot \sqrt{(\dot{s}_x(t; i,j) + \dot{s}^*_x(t + \Delta t; i,j))^2 + \left(\dot{s}_y(t; i,j) + \dot{s}^*_y(t + \Delta t; i,j)\right)^2}/2,
\end{aligned}
$$

where $S^*_\nu\ (t + \Delta t;\ k,\ m)$ are computed from $\dot{s}^*_\nu\ (t + \Delta t;\ i,\ j)$ using FFT.

[97] 4. Find the second prediction of slip rates, $\dot{s}^{**}_\nu\ (t + \Delta t;\ i, j)$, corresponding to the predicted slips $\ell^{**}\ (t + \Delta t;\ i, j)$ and functionals $f^{**}_\nu(t + \Delta t;\ i,\ j)$. The consideration is analogous to stage 2 (where all quantities with one star are replaced with quantities with two stars).

[98] 5. Treat the second predictions as the values of the field variables at time $t + \Delta t$. Store tangential discontinuities (slips) $s_\nu(t + \Delta t;\ i, j)$, the Fourier coefficients of slips $S_\nu\ (t + \Delta t;\ k,\ m)$, slip rates $\dot{s}_\nu\ (t + \Delta t;\ i, j)$, $\nu = x, y$, and slip path length $\ell\ (t + \Delta t;\ i,\ j)$ for use in the next time step. In addition, supplement the slip rate history by storing the value $(\dot{S}_\nu\ (t;\ k,\ m) + \dot{S}^*_\nu\ (t + \Delta t;\ k,\ m))/2$ for the time interval $(t,\ t + \Delta t]$ so that the slip rates are now known, in terms of their Fourier coefficients, for (discretized) prior time t', $0 < t' < t + \Delta t$.

[99] **Acknowledgments.** The authors thank Ruth Harris and Ralph Archuleta for organizing the Southern California Earthquake Center (SCEC) Spontaneous Rupture Code-Validation project, which provided the initial impetus to compare the BI and DFM methods. Jean Paul Ampuero, Peter Moczo, and Joe Andrews provided very helpful reviews, leading to improvements in the manuscript. Jean Virieux pointed out connections between the DFM scheme and other finite difference methods. This work was supported by the National Science Foundation, under grants ATM-0325033 and EAR-0122464 (SCEC Community Modeling Environment Project), and by SCEC. SCEC is funded by NSF Cooperative Agreement EAR-0106924 and USGS Cooperative Agreement 02HQAG0008. This is SCEC contribution 907.

References

Abramowitz, M., and I. Stegun (1964), *Handbook of Mathematical Functions*, Natl. Inst. of Stand. and Technol., Gaithersburg, Md.

Andrews, D. J. (1976), Rupture propagation with finite stress in antiplane strain, *J. Geophys. Res.*, *81*, 3575–3582.

Andrews, D. J. (1985), Dynamic plane-strain shear rupture with a slip-weakening friction law calculated by a boundary integral method, *Bull. Seismol. Soc. Am.*, *75*, 1–21.

Andrews, D. J. (1999), Test of two methods for faulting in finite-difference calculations, *Bull. Seismol. Soc. Am.*, *89*, 931–937.

Andrews, D. J. (2004), Rupture models with dynamically-determined breakdown displacement, *Bull. Seismol. Soc. Am.*, *94*, 769–775.

Andrews, D. J. (2005), Rupture dynamics with energy loss outside the slip zone, *J. Geophys. Res.*, *110*, B01307, doi:10.1029/2004JB003191.

Aochi, H., E. Fukuyama, and M. Matsu'ura (2000), Selectivity of spontaneous rupture propagation on a branched fault, *Geophys. Res. Lett.*, *27*, 3635–3638.

Archuleta, R. J., and S. M. Day (1980), Dynamic rupture in a layered medium: The 1966 Parkfield Earthquake, *Bull. Seismol. Soc. Am.*, *70*, 671–689.

Ben-Zion, Y., and J. R. Rice (1997), Dynamic simulations of slip on a smooth fault in an elastic solid, *J. Geophys. Res.*, *102*, 17,771–17,784.

Bizzarri, A., M. Cocco, D. J. Andrews, and E. Boschi (2001), Solving the dynamic rupture problem with different numerical approaches and constitutive laws, *Geophys J. Int.*, *144*, 656–678.

Broberg, K. B. (1999), *Cracks and Fracture*, Elsevier, New York.

Brune, J. N., and A. Anooshehpoor (1998), A physical model of the effect of a shallow weak layer on strong ground motion for strike-slip ruptures, *Bull. Seismol. Soc. Am.*, *88*, 1070–1078.

Campillo, M., and I. R. Ionescu (1997), Initiation of antiplane shear instability under slip dependent friction, *J. Geophys. Res.*, *102*, 20,363–20,371.

Chen, X., and H. Zhang (2004), Spontaneous rupture dynamics of a planar fault with arbitrary dipping orientation embedded in 3-D elastic half-space, *Eos Trans. AGU*, *85*(47), Fall Meet. Suppl., Abstract S12A-04.

Cochard, A., and R. Madariaga (1994), Dynamic faulting under rate-dependent friction, *Pure Appl. Geophys.*, *142*, 419–445.

Cochard, A., and J. R. Rice (2000), Fault rupture between dissimilar materials: Ill-posedness, regularization, and slip-pulse response, *J. Geophys. Res.*, *105*, 25,891–25,907.

Cruz-Atienza, V. M., and J. Virieux (2004), Dynamic rupture simulation of non-planar faults with a finite-difference approach, *Geophys. J. Int.*, *158*, 939–954.

Dalguer, L. A., and S. M. Day (2004), Split nodes and fault zone models for dynamic rupture simulation, *Eos Trans. AGU*, *85*(47), Fall Meet. Suppl., Abstract S41A-0944.

Dalguer, L. A., K. Irikura, J. D. Riera, and H. C. Chiu (2001), The importance of the dynamic source effects on strong ground motion during the 1999 Chi-Chi, Taiwan, earthquake: Brief interpretation of the damage distribution on buildings, *Bull. Seismol. Soc. Am.*, *91*, 1112–1127.

Dalguer, L. A., K. Irikura, and J. D. Riera (2003a), Simulation of tensile crack generation by three-dimensional dynamic shear rupture propagation during an earthquake, *J. Geophys. Res.*, *108*(B3), 2144, doi:10.1029/2001JB001738.

Dalguer, L. A., K. Irikura, and J. D. Riera (2003b), Generation of new cracks accompanied by the dynamic shear rupture propagation of the 2000 Tottori (Japan) earthquake, *Bull. Seismol. Soc. Am.*, *93*, 2236–2252.

Das, S. (1980), A numerical method for determination of source time functions for general three-dimensional rupture propagation, *Geophys. J. R. Astron. Soc.*, *62*, 591–604.

Das, S., and K. Aki (1977), Fault planes with barriers: A versatile earthquake model, *J. Geophys. Res.*, *82*, 5648–5670.

Das, S., and B. V. Kostrov (1988), An investigation of the complexity of the earthquake source time function using dynamic faulting models, *J. Geophys. Res.*, *93*, 8035–8050.

Day, S. M. (1977), Finite element analysis of seismic scattering problems, Ph.D. dissertation, Univ. of Calif., San Diego.

Day, S. M. (1982a), Three-dimensional finite difference simulation of fault dynamics: rectangular faults with fixed rupture velocity, *Bull. Seismol. Soc. Am.*, *72*, 705–727.

Day, S. M. (1982b), Three-dimensional simulation of spontaneous rupture: the effect of nonuniform prestress, *Bull. Seismol. Soc. Am.*, *72*, 1881–1902.

Day, S. M. (1991), Numerical simulation of fault propagation with interface separation (abstract), *Eos Trans. AGU*, *72*, 486.

Day, S. M., and G. P. Ely (2002), Effect of a shallow weak zone on fault rupture: Numerical simulation of scale-model experiments, *Bull Seismol. Soc. Am.*, *92*, 3022–3041.

Dieterich, J. H. (1979), Modeling of rock friction: 1. Experimental results and constitutive equations, *J. Geophys. Res.*, *84*, 2161–2168.

Ely, G. P. (2001), Simulating the effect of a shallow weak zone on near-source ground motion, M.S. thesis, San Diego State Univ., San Diego, Calif.

Freund, L. B. (1989), *Dynamic Fracture Mechanics*, Cambridge Univ. Press, New York.

Geubelle, P., and J. R. Rice (1995), A spectral method for 3D elastodynamic fracture problems, *J. Mech. Phys. Solids*, *43*, 791–824.

Gustafsson, B., H.-O. Kreiss, and J. Oliger (1995), *Time Dependent Problems and Difference Methods*, John Wiley, New York.

Harris, R. A., et al. (2004), The source physics of large earthquakes: Validating spontaneous rupture methods, *Eos Trans. AGU*, *85*(47), Fall Meet. Suppl., Abstract S12A-05.

Hughes, T. J. R. (1987), *The Finite Element Method, Linear Static and Dynamic Finite Element Analysis*, Prentice-Hall, Upper Saddle River, N. J.

Ida, Y. (1972), Cohesive force across the tip of a longitudinal-shear crack and Griffith's specific surface energy, *J. Geophys. Res.*, *77*, 3796–3805.

Kame, N., and T. Yamashita (1999), Simulation of the spontaneous growth of a dynamic crack without constraints on the crack tip path, *Geophys. J. Int.*, *139*, 345–358.

Kase, Y., and S. M. Day (2004), Spontaneous rupture process on a bending Fault, *Eos Trans. AGU*, *85*(47), Fall Meet. Suppl., Abstract S41A-0945.

Kosloff, D., and G. A. Frazier (1978), Treatment of hourglass patterns in low order finite element codes, *Numer. Anal. Methods Geomech.*, *2*, 57–72.

Lachenbruch, A. H. (1980), Frictional heating, fluid pressure and the resistance to fault motion, *J. Geophys. Res.*, *85*, 6097–6112.

Lapusta, N., and J. R. Rice (2003), Nucleation and early seismic propagation of small and large events in a crustal earthquake model, *J. Geophys. Res.*, *108*(B4), 2205, doi:10.1029/2001JB000793.

Lapusta, N., J. R. Rice, Y. Ben-Zion, and G. Zheng (2000), Elastodynamic analysis for slow tectonic loading with spontaneous rupture episodes on faults with rate- and state-dependent friction, *J. Geophys. Res.*, *105*, 23,765–23,789.

Madariaga, R., K. B. Olsen, and R. J. Archuleta (1998), Modeling dynamic rupture in a 3-D earthquake fault model, *Bull. Seismol. Soc. Am.*, *88*, 1182–1197.

Mase, C. W., and L. Smith (1985), Pore-fluid pressures and frictional heating on a fault surface, *Pure Appl. Geophys.*, *122*, 583–607.

Mase, C. W., and L. Smith (1987), Effects of frictional heating on the thermal, hydrologic, and mechanical response of a fault, *J. Geophys. Res.*, *92*, 6249–6272.

Miyatake, T. (1980), Numerical simulations of earthquake source process by a three-dimensional crack model, part 1. Rupture process, *J. Phys. Earth*, *28*, 565–598.

Moczo, P., J. O. A. Robertsson, and L. Eisner (2006), The finite-difference time-domain method for modeling of seismic wave propagation, in *Advances in Wave Propagation in Heterogeneous Earth*, *Adv. Geophys.*, vol. 48, edited by R.-S. Wu and V. Maupin, edited by R. Dmowska, Elsevier, New York, in press.

Palmer, A. C., and J. R. Rice (1973), The growth of slip surfaces in the progressive failure of overconsolidated clay slopes, *Proc. R. Soc. London, Ser. A*, *332*, 537.

Perrin, G., J. R. Rice, and G. Zheng (1995), Self-healing slip pulse on a frictional surface, *J. Mech. Phys. Solids*, *43*, 1461–1495.

Press, W. H., B. P. Flannery, S. A. Teukolsky, and W. T. Vetterling (1986), *Numerical Recipes in FORTRAN: The Art of Scientific Computing*, Cambridge Univ. Press, New York.

Ranjith, K., and J. R. Rice (2001), Slip dynamics at an interface between dissimilar materials, *J. Mech. Phys. Solids*, *49*, 341–361.

Rice, J. R. (1968), A path independent integral and the approximate analysis of strain concentration by notches and cracks, *J. Appl. Mech.*, *35*, 379–386.

Rice, J. R. (1980), The mechanics of earthquake rupture, in *Physics of the Earth's Interior*, *Proc. Int. Sch. Phys. Enrico Fermi, Course 78*, edited by A. M. Dziewonski and E. Boschi, pp. 555-649, Elsevier, New York.

Rice, J. R. (1999), Flash heating at asperity contacts and rate-dependent friction, *Eos Trans. AGU*, *80*(46), Fall Meet. Suppl., F681.

Ruina, A. L. (1983), Slip instability and state variable friction laws, *J. Geophys. Res.*, *88*, 10,359–10,370.

Wood, W. L. (1990), *Practical Time-Stepping Schemes*, Clarendon, Oxford, U.K.

Zhang, W. B., T. Iwata, K. Irikura, A. Pitarka, and H. Sekiguchi (2004), Dynamic rupture process of the 1999 Chi-Chi, Taiwan, earthquake, *Geophys. Res. Lett.*, *31*, L10605, doi:10.1029/2004GL019827.

L. A. Dalguer and S. M. Day, Department of Geological Sciences, San Diego State University, 5500 Campanile Drive, San Diego, CA 92182, USA. (day@moho.sdsu.edu)

N. Lapusta, Division of Geological and Planetary Sciences, California Institute of Technology, Pasadena, CA 91125, USA.

Y. Liu, Division of Engineering and Applied Science, California Institute of Technology, Pasadena, CA 91125, USA.